Journal of Catalysis 280 (2011) 274–288

Contents lists available at ScienceDirect

Journal of Catalysis

journal homepage: www.elsevier.com/locate/jcat

New insights into the role of the electronic properties of oxide promoters in Rh-catalyzed selective synthesis of oxygenates from synthesis gas

Gonzalo Prieto [a], Patricia Concepción [a], Agustín Martínez [a,*], Ernest Mendoza [b]

[a] Instituto de Tecnología Química, UPV-CSIC, Avda. de los Naranjos s/n, 46022 Valencia, Spain
[b] Centre de Recerca en Nanoenginyeria, Universitat Politècnica de Catalunya, c/Pascual i Vila 15, 08028 Barcelona, Spain

ARTICLE INFO

Article history:
Received 29 December 2010
Revised 11 March 2011
Accepted 27 March 2011
Available online 13 May 2011

Keywords:
Synthesis gas
Oxygenates
Rhodium
Promoters
Electronic properties
Model catalysts
At-work CO-FTIR

ABSTRACT

A series of 2.5% Rh/M@Al_2O_3 model catalysts were prepared by supporting Rh on high-area γ-Al_2O_3, resulting in a surface covered by a *monolayer* (4.5–7 atoms/nm^2) of MO_x promoter oxides (M = Fe, V, Nb, Ta, Ti, Y, Pr, Nd, Sm). The catalysts were extensively characterized and evaluated for the conversion of synthesis gas to oxygenates at 553 K, 5.0 MPa, H_2/CO = 1, and space velocity adjusted to attain CO conversion around 15%. The broad range of products formed depending on the specific promoter were, for the first time, quantitatively described using the *selectivity parameter* (Φ) defined here, which indicates, for a given reaction product, the contribution of carbon atoms derived from dissociative (C_{dis}) and nondissociative (C_{ins}) activation of CO. Both the catalytic activity and, more interestingly, the selectivity pattern given by the Φ parameter were correlated with the electronic properties of the MO_x promoters (i.e., electron-donating/electron-withdrawing capacity) for an extensive series of catalysts. *Low-temperature* and *at-work* CO-FTIR experiments suggested that the high activity and hydrocarbon selectivity displayed by catalysts promoted by more electron-withdrawing (acidic) oxide promoters (e.g., TaO_x) were related to a higher proportion of bridged $Rh_2(CO)_B$ adsorption sites and to a higher electron density (i.e., a higher electron back-donation ability) of the Rh^0 surface sites, both factors promoting CO dissociation events. In contrast, linear CO adsorption on Rh^0 sites displaying decreased electron back-donation in catalysts promoted by electron-donating (basic) oxides (e.g., PrO_x, SmO_x) was likely related to nondissociative CO activation and thus to the selective formation of oxygenates. TEM, XPS, and CO-FTIR results pointed to differences in morphology, rather than size or partial electronic charge, of the nanosized Rh^0 crystallites as the likely cause for the different proportions of CO adsorption sites. The Rh^0 NP morphology, both as-reduced and at-work, is a function of the electronic properties of the underlying promoter oxide.

1. Introduction

Higher (C_{2+}) oxygenates are highly demanded energy carriers and platform chemicals. For instance, the current ethanol market is witnessing a sparked growth, with a forecast worldwide production of around 60×10^6 t/year in 2012, due to its applications as transportation fuel, source of renewable hydrogen for fuel cells, and feedstock for the synthesis of chemicals such as ethylene [1,2]. In addition, longer-chain (C_3—C_6) aliphatic alcohols hold great industrial interest as fuel additives, high-energy–density fuels, and raw materials for polymers and fine chemicals [3]. Moreover, carboxylic compounds such as acetic acid and methyl and ethyl acetates are valuable oxygenates that find application as raw chemicals and solvents in a wide range of industries, with a current combined world demand exceeding 8×10^6 t/year.

Dwindling crude oil reserves and concerns related to competition with the food industry are factors encouraging the development of effective catalytic processes to produce higher oxygenates from abundant and/or renewable resources, as an alternative to petroleum refining and edible-crop-consuming fermentative routes [4–6]. The catalytic conversion of synthesis gas (*syngas*) derived from stranded natural gas reservoirs or biomass (including lignocellulosic biomass) into higher oxygenates has long been known. Although the process has not yet been commercially implemented, renewed industrial and scientific interest is being experienced nowadays, as attested by considerable governmental and private strategic research investments.

Rh-based catalysts have been known to be effective for the selective synthesis of C_{2+} oxygenates (denoted hereafter as SSO) from syngas since the middle 1970s [7]. Although this catalytic system shows promise due to its high selectivity to linear C_{2+} oxygenates, particularly to ethanol, as well as to the fact that it does not require the presence of sulfur in the syngas feed stream,

* Corresponding author. Fax: +34 963877808.
E-mail address: amart@itq.upv.es (A. Martínez).

0021-9517/$ - see front matter © 2011 Elsevier Inc. All rights reserved.
doi:10.1016/j.jcat.2011.03.025

its commercial application has been hindered mainly by the relatively low catalytic yields and the high cost and limited availability of Rh. Thus, a deeper understanding of the nature of active/selective sites, based on which novel optimized catalysts could be synthesized, seems crucial for improving the commercial competitiveness of the Rh-catalyzed SSO.

Apart from commercial considerations, the use of Rh-based catalysts for the SSO is of particular scientific interest due to a singular and drastic *promotion effect*, according to which the addition of transition metal or lanthanide oxides as promoters is essential to attain acceptable catalytic activity and selectivity to the desired oxygenates. It is known that unpromoted Rh nanoparticles (NPs) supported on the most common SiO_2 or Al_2O_3 carriers show low activity and very poor selectivity to oxygenates [8]. In contrast, the incorporation of promoters such as iron, either intentionally or coming from impurities in the support [9], dramatically changes the catalytic behavior by increasing the activity and selectivity to C_{2+} alcohols, especially ethanol. The search for the optimum promoter, or combination of promoters, has led to a vast amount of scientific work and several reviews during the past two decades [2,6]. For instance, Ichikawa [10,11] studied the promoting effect of several transition metal and lanthanide oxides in their dual role of promoter and catalytic support for Rh NPs and concluded that oxides displaying a slightly basic character (so-called *amphoteric* oxides) such as La_2O_3, Cr_2O_3, TiO_2, and ThO_2 were the most effective in increasing the ethanol yield. On the other hand, Du et al. [12] found that among several lanthanide oxide promoters (La, Ce, Pr, Nd, and Sm), CeO_x and PrO_x lead to the highest ethanol selectivity in SiO_2-supported Rh catalysts. More recently, Goodwin and co-workers [13] found a synergistic promoting effect of the combined addition of V and La oxides to a Rh/SiO_2 catalyst, leading to higher CO hydrogenation activity and selectivity to ethanol (and in general to C_{2+} oxygenates) than for any of the monopromoted counterparts. In addition, some contradictory results can also be found in the previous literature dealing with promotion effects in Rh-catalyzed SSO. For instance, while some studies concluded that MnO_x was a suitable promoter for Rh in the SSO [14,15], others found that the addition of MnO_x to a Rh/SiO_2 catalyst adversely affected its activity and selectivity to alcohols [16]. The complexity of the promoted Rh system is further evidenced by marked sensitivity of the selectivity pattern to subtle variations in the nature of the oxidic promoters. Thus, while Rh–Ir–Mn–Li/SiO_2 catalysts displayed high selectivity to acetic acid [17], Rh–Fe–Mn–Li/SiO_2 systems were shown to produce ethanol as the major oxygenate [18]. Similarly, Sachtler et al. observed a shift in the selectivity from acetic acid to ethanol as the major oxygenate upon incorporation of small amounts of iron into a Rh/NaY catalyst [19,20]. Besides its nature, the amount of oxidic promoter was also seen to impact the catalyst performance. Generally, both catalytic activity and selectivity went through a maximum with increasing promoter-to-Rh atomic ratio, which was interpreted in terms of decoration and, in the limit, occlusion of Rh NPs by the oxidic promoter phases [21]. Nevertheless, the adequate promoter/Rh ratio appears to be dependent on the specific catalytic system, since optimum Fe/Rh atomic ratios as disparate as 2.3 for Rh–Fe/SiO_2 [22], 4.6 for Rh–Fe/TiO_2 [22], and 9.2 for Rh–Fe/Al_2O_3 [23] catalysts are reported, probably because of distinct levels of intimacy between the promoter and the Rh phase.

These results clearly point to the need for systematic studies aimed at elucidating the relationships between the nature of the oxidic promoters and the catalytic behavior, particularly the product selectivity. Gaining insight into the true role of catalytic promoters and their optimum electronic requirements will surely be crucial for the design of improved generations of Rh-based catalysts. Somorjai and co-workers [24] carried out an exhaustive study employing *inverse model* catalysts consisting of Rh^0 foils surface-decorated with patches of a transition metal oxide promoter for an extensive series of oxides (AlO_x, TiO_x, VO_x, FeO_x, ZrO_x, NbO_x, TaO_x, and WO_x) and found that the Lewis acidity of the promoter phase was crucial in determining the CO hydrogenation activity under methanation conditions and, thus, no consideration could be made in terms of product selectivity. Moreover, it has to be taken into account that in real catalysts Rh is present as a dispersed phase which, a priori, might behave differently than the Rh monocrystals in these *inverse model* catalysts.

It is widely accepted that the promoter/Rh boundary plays a key role in creating the required active sites for the SSO [24]. Thus, special care has to be taken in dealing with model catalytic systems to well define, and ideally maximize, the contact surface between these two phases, something which can hardly be controlled by employing conventional preparative techniques such as co-impregnation of Rh and the promoter's precursors. Additionally, the size of the metallic Rh NPs is another parameter to be considered, since it has been proved to influence the catalytic properties [25–27]. Hence, simply employing different metal oxides in the dual role of support and promoter will not generally lead to model catalysts displaying homogeneous metal dispersion, due to the great variability of textures among different oxides [28].

We present a systematic and exhaustive study on the effect of the electronic properties of oxidic promoters on the catalytic properties of model nanoparticulated Rh catalysts for the SSO. For the sake of homogeneity in their textural properties while maximizing the promoter-Rh contact boundary, the set of model catalysts was prepared by incorporating the Rh precursor onto high-surface supports consisting of a common porous carrier (γ-Al_2O_3) having its surface covered by a *monolayer* of the corresponding MO_x promoter oxide [23]. To attain a representative vision of the whole study space, a broad series of transition metal and lanthanide oxides (MO_x), displaying a wide range of electronic properties, were studied as catalytic promoters.

2. Experimental

2.1. Synthesis of catalysts

2.1.1. Synthesis of M@Al_2O_3 catalytic supports

The series of M@Al_2O_3 catalytic supports studied consisted of several metal oxides MO_x (where M = Fe(III), V(V), Nb(V), Ta(V), Ti(IV), Y(III), Pr(III), Nd(III), and Sm(III)) dispersed on the surface of γ-Al_2O_3. These materials were carefully prepared, targeting high dispersions for the MO_x species, ideally as bidimensional supported oxides, at surface coverages corresponding to *monolayer* saturation in each case. The common γ-Al_2O_3 carrier was obtained by calcination of high-purity commercial pseudo-boehmite, Pural-SB (Sasol Materials), at 773 K for 10 h in a muffle oven. Prior to the incorporation of metal precursors, the γ-Al_2O_3 carrier was dried at 423 K for 12 h.

The metal loading was adjusted in each case to attain nominal *monolayer* (ML) coverage on the γ-Al_2O_3 surface (based on the B.E.T. surface area of the dehydrated alumina of 205 m^2/g) by the MO_x promoter, according to previously published results where the ML saturation coverage was determined for several γ-Al_2O_3-supported oxides [23,29–33]. These *monolayer* coverages were within the range of 4.5–5 M/nm^2 for most of the studied oxides, though in the case of VO_x, the required saturation coverage was 7 V/nm^2 due to the special packing of oxygen atoms in supported polyvanadates [29].

The loading of the γ-Al_2O_3 support with transition metal precursors (Fe, V, Nb, Ta, Ti, Y) was accomplished by impregnation with alcoholic solutions of organic precursors such as alkoxides or acetylacetonate (2,4-pentanedionate), which are the preferred

Table 1
Nominal *monolayer* surface coverage, nature, purity, and suppliers of metal precursors and solvents used in the preparation of $M@Al_2O_3$ catalytic supports.

Support	Promoter (M)	δ (at/nm^2)[a]	Precursor of M	Solvent[b]
$Fe@Al_2O_3$	Fe	4.5	$Fe(C_5H_7O_2)_3$ 99.9%+ (Aldrich)	Methanol (Anh)
$V@Al_2O_3$	V	7.0	$VO(OC_3H_7)_3$ (Aldrich)	Ethanol (Anh)
$Nb@Al_2O_3$	Nb	5.0	$Nb(OC_2H_5)_5$, 99.95% (Aldrich)	Ethanol (Anh)
$Ta@Al_2O_3$	Ta	5.0	$Ta(OC_2H_5)_5$, 99.98% (Aldrich)	Ethanol (Anh)
$Ti@Al_2O_3$	Ti	4.5	$Ti(OC_2H_5)_4$, >95% (Alfa-Aesar)	Ethanol (Anh)
$Y@Al_2O_3$	Y	4.5	$Y(C_5H_7O_2)_3$ (Alfa-Aesar)	2 vol.% CH_3COOH/methanol
$Pr@Al_2O_3$	Pr	4.5	$Pr(NO_3)_3{\cdot}5H_2O$ (Aldrich)	H_2O
$Nd@Al_2O_3$	Nd	4.5	$Nd(NO_3)_3{\cdot}6H_2O$ (Aldrich)	H_2O
$Sm@Al_2O_3$	Sm	4.5	$Sm(NO_3)_3{\cdot}6H_2O$ (Aldrich)	H_2O

[a] Nominal surface coverage for monolayer saturation.
[b] Anh: anhydrous.

metal precursors to attain monolayer dispersions for these supported oxides [34,35]. Experimentally, the γ-Al_2O_3 carrier was dehydrated in a three-neck flask at 623 K for 20 h. Afterward, an alcoholic solution of the corresponding organic metal precursor, previously prepared under anhydrous atmosphere in a globe box, was injected onto the dehydrated support while the flask was flushed with dry N_2. The amount of dissolved metal precursor was set to yield the metal loading corresponding to the desired nominal coverage. The resulting suspension was vigorously stirred at 313 K under protective dry N_2, and subsequently the solvent was evaporated in a rotary evaporator. The obtained solid was dried at 333 K in an oven for 10 h and finally calcined in flowing air at 773 K for 3 h (heating rate 3 K min^{-1}, GHSV 20 ml g^{-1} min^{-1}).

In contrast to the case of most transition metal oxides, the achievement of 2D dispersions of lanthanide oxides on oxidic carriers was shown to require the use of aqueous solutions of nitrate precursors instead of anhydrous organic solutions of organic compounds [36,37]. Thus, in the present study, the synthesis of catalytic supports comprising a monolayer of lanthanide (Pr, Nd, Sm) oxides was performed by incipient wetness impregnation of the dried γ-Al_2O_3 support with an aqueous solution of the corresponding nitrate precursor. The impregnated solids were then dried at 373 K in an oven for 10 h and finally calcined in flowing air at 773 K for 3 h (heating rate 3 K/min, GHSV 20 ml g^{-1} min^{-1}).

Table 1 shows the nominal surface coverage (δ) as well as the nature of the metal precursor and the solvent employed for each specific preparation.

2.1.2. Synthesis of $Rh/M@Al_2O_3$ catalysts

The series of $Rh/M@Al_2O_3$ catalysts was prepared by incipient wetness impregnation of the corresponding calcined $M@Al_2O_3$ supports (previously dried at 423 K for 12 h) with an aqueous solution of $RhCl_3{\cdot}xH_2O$ (34.7 wt.% Rh as determined by ICP-OES, metallic purity >97%, Sigma–Aldrich). The impregnation was carried out in two consecutive steps with a 30-min drying step in between at 333 K. After the second impregnation step, the solids were dried at 373 K for 12 h and then calcined in a muffle oven at 673 K for 4 h (heating rate 2 K/min). The amount of Rh precursor was set in all cases to get a 2.5 wt.% nominal Rh loading. Additionally, a Rh/Li–$Ta@Al_2O_3$ catalyst was prepared following the above procedure but employing a mixed aqueous solution of $RhCl_3{\cdot}xH_2O$ and $LiNO_3$ (ultrapurum, Sigma–Aldrich). In this case, the amount of Li precursor was set to obtain a nominal Li loading of 0.2 wt.%, corresponding to a surface coverage on the $Ta@Al_2O_3$ support (B.E.T. 176 m^2/g) of 1.0 Li/nm^2.

2.2. Characterization methods

Chemical analysis was performed by ICP-OES. The samples (ca. 20 mg) were dissolved in a HNO_3/HF/HCl solution (1:1:3 volume ratio) before analysis in a Varian 715-ES ICP-optical emission spectrometer. In turn, the lanthanide content in certain samples was also evaluated by X-ray fluorescence spectroscopy (XRF) using a Philips MiniPal 25 fm setup. X-ray diffraction (XRD) patterns of calcined solids were obtained in a Philips X'pert diffractometer using monochromatic Cu Kα radiation. The N_2 adsorption isotherms were measured in a Micromeritics ASAP 2000 equipment. The samples (ca. 200 mg) were degassed at 673 K for 24 h prior to analysis. Specific surface areas were calculated using the B.E.T. approach, while average pore sizes and pore size distributions were obtained by applying the B.J.H. formalism to the adsorption branch of the isotherms.

H_2 temperature-programmed reduction (H_2 TPR) profiles of $M@Al_2O_3$ supports and $Rh/M@Al_2O_3$ catalysts were obtained in a Micromeritics Autochem 2910 apparatus. About 100 mg of sample (particle size 0.25–0.42 mm) was initially flushed with Ar at room temperature (RT) for 30 min; then the gas was switched to 10 vol.% H_2/Ar and the temperature was linearly increased to 1173 K at a heating rate of 10 K/min. A downstream 2-propanol/$N_{2(liq.)}$ trap (193 K) was used to retain water generated in the reductions. The solids containing YO_x or lanthanide oxides were previously submitted to in situ decarbonation consisting of calcining the sample in flowing synthetic air at 873 K for 2 h in the U-shaped cell. In all cases, the H_2 consumption rate was monitored in a thermal conductivity detector (TCD) previously calibrated using the reduction of CuO as a reference.

Transmission electron microscopy (TEM) of selected samples was performed in a JEOL JEM-2011 microscope operated at 200 kV. Before observation, the catalysts were reduced in flowing pure H_2 at 573 K for 6 h and stored at room temperature under a <1 vol.% O_2/N_2 atmosphere until sample preparation for microscopy. In all cases, the TEM specimen was prepared by suspending the solid in ethanol, ultrasonicating for 1 min, and placing a drop on a holey film carbon-coated copper grid.

The electronic properties of the MO_x promoter species in $M@Al_2O_3$ catalytic supports were studied by means of DR UV–vis spectroscopy coupled with adsorption of alizarine (1,2-dihydroxy-9,10-anthracenodione), following the methodology recently developed by Jeong et al. [38]. As previously shown by these authors, the lowest-energy intramolecular charge-transfer energy *E*(IMCT) of the adsorbed alizarine is a very sensitive parameter, according to which a universal scale of electron-withdrawing–donating power (or acidity–basicity according to the Lewis concept) can be established for metal chalcogenides, including lanthanide oxides [38]. Experimentally, 150 mg of the calcined $M@Al_2O_3$ support was suspended in 20 ml of anhydrous ethanol, and then 20 ml of a 0.125 M ethanolic solution of alizarine was added. The resulting suspension was vigorously stirred for 10 min and then the solid was filtered, abundantly washed with ethanol until dye was absent in the mother liquids, and dried under vacuum for 12 h. In certain cases, the $M@Al_2O_3$ supports were initially submitted to a decarbonation treatment (specifically those

containing Y, Pr, Nd, and Sm) at 873 K in flowing air for 2 h, or to a reduction treatment in flowing H_2/N_2 (V@Al_2O_3 and Fe@Al_2O_3), and kept under N_2 until alizarine adsorption. The DR UV–vis spectra were recorded at room temperature in a Cary 5 spectrometer using $BaSO_4$ as a reflectance standard.

CO chemisorption experiments for selected Rh/M@Al_2O_3 catalysts were performed in a Micromeritics ASAP 2010C device. About 300 mg of sample was flushed with He at 393 K for 1 h and then reduced in situ at 573 K for 6 h in flowing pure H_2 (heating rate 1 K/min). After reduction, the cell was evacuated at 1.3 Pa and the sample allowed to cool under vacuum. A first chemisorption isotherm was then recorded at 308 K, after which the cell was evacuated at the same temperature and a second isotherm registered. The amount of irreversibly chemisorbed CO was calculated by extrapolating the difference isotherm (total-reversible) to zero CO pressure.

X-ray photoemission spectra (XPS) were recorded in a SPECS spectrometer equipped with a Phoibos 150 9MCD detector using a nonmonochromatic X-ray source (Al and Mg) operating at 200 W. The calcined samples were pressed into a small disk and evacuated in the prechamber of the spectrometer at 1×10^{-9} mbar. Selected catalysts were additionally studied after reduction in situ in flowing H_2 at 573 K for 6 h followed by evacuation at 1×10^{-8} mbar. For the XPS measurements in situ, a flow of 50 mL/min of syngas (CO/H_2/Ar in a 45/45/10 volume ratio) was established through the prereduced catalyst while the temperature was raised to 553 K (the temperature applied here for the SSO catalytic experiments) and kept there for 2.5 h. Afterward, the samples were evacuated at RT and transferred to the analysis chamber of the spectrometer. Binding energies (BE) of the detected peaks were corrected by charging effects using the Al2*p* signal (coming from the Al_2O_3 carrier) as reference (Al2*p* = 74.5 eV), and peak intensities were calculated after nonlinear Shirley-type background subtraction and corrected by the transmission function of the spectrometer. Additionally, the intensity ratio (Rh3$d_{5/2}$)/(Al2*p*) was used to estimate the Rh nanoparticle size in selected as-reduced catalysts by applying the model proposed by Kerkhof and Moulijn [39] and assuming no attenuation by the MO_x monolayer. Theoretical cross section (σ) values proposed by Scofield [40], inelastic mean free path (λ) values according to Seah [41], and an instrumental efficiency factor dependent on the kinetic energy (KE), as provided by the instrument manufacturer, were used in the calculations. The CasaXPS software was used for spectra deconvolution.

Low-temperature and *at-work* infrared spectroscopic (FTIR) experiments were performed in a Bio-Rad FTS-40A spectrometer using, respectively, a homemade stainless steel cell and a quartz cell fitted with KRS-5 windows, both connected to a vacuum dosing system. Before each experiment, the catalysts were pressed into self-supported wafers (5–10 mg/cm^2) and reduced in situ in the IR cell under flowing pure H_2 at 573 K for 2 h. After the reductive pretreatment, the samples were degassed under vacuum (ca. 10^{-5} mbar) at 623 K (50 K above the reduction temperature) to allow the displacement of any H_2 adsorbed on the metal surface and then cooled down to RT under vacuum. For low-temperature CO adsorption experiments, the in situ reduced samples were cooled to 77 K followed by CO dosing at increasing pressure (0.4–8.5 mbar) and recording the IR spectrum after each dosage. After CO dosing, the samples were evacuated and the spectra collected at increasing temperatures under dynamic vacuum conditions (10^{-5} mbar) for 24 h, in order to gain insight into the stability of the different adsorbed species upon evacuation. For at-work IR experiments, the reduced samples were exposed to a flow (50 ml/min) of syngas ($CO:H_2$:Ar in a volume ratio of 45:45:10) at RT for 1 h to ensure a homogeneous atmosphere in the cell. Then the temperature was increased stepwise from RT to 553 K and maintained for 3 h. The IR spectra were recorded after 5 min at each temperature and after 10, 30, 60, 120, and 180 min on stream at the final temperature (553 K). After the reaction, the catalysts were progressively degassed in order to study the relative stability of the adsorbed species.

2.3. Catalytic tests

The catalytic experiments were carried out in a downflow fixed-bed 310-stainless steel reactor. The catalytic system was equipped with a high-pressure gas Purifilter (Matheson Trigas) at the reactor inlet in order to retain metal carbonyls coming from the pressurized gas cylinders [8,23]. In a typical experiment, the reactor was loaded with 1.0–1.5 g of catalyst in the calcined form (pellet size 0.25–0.42 mm) previously diluted with the required amount of SiC (0.6–0.8 mm) to attain a constant bed volume of 5.0 cm^3. Then the catalyst was reduced in situ at atmospheric pressure in flowing pure H_2 (133 cm^3 min^{-1} g_{cat}^{-1}) at 573 K for 6 h (1 K/min). After reduction, the temperature was lowered to 373 K under the flow of H_2, and subsequently a flow of a mixture of CO, H_2, and Ar ($CO:H_2$:Ar volume ratio of 45:45:10, Ar used as internal standard for GC analyses) was established through the reactor, the reaction pressure slowly increased to 5.0 MPa, and the temperature raised to 553 K at a rate of 4 K/min. Under these conditions, pseudo-steady catalytic behavior was usually attained at time on stream (TOS) greater than 7–8 h. A constant gas hourly space velocity (GHSV) of 2.8×10^3 cm^3_{syngas} g_{cat}^{-1} h^1 was applied for all catalysts during the first 7–8 h on stream (transient period) and then the space velocity was adjusted in each case to attain a pseudo-steady CO conversion of 15 ± 3%. The temperature in the catalyst bed was controlled to 553 ± 1 K by means of two independent electric heating zones, with the corresponding temperature controllers connected to thermocouples located at different positions inside the catalytic bed. An additional moveable thermocouple was used to verify the absence of longitudinal temperature gradients and hot spots along the catalyst bed. The product stream leaving the reactor was depressurized and analyzed on line at periodic intervals in a GC (Varian 3800) equipped with three columns and TCD and FID detectors [42]. The transfer line between the reactor and the GC was maintained at 473 K. For all the catalytic experiments reported here, carbon mass balances of 100 ± 2% were obtained. Product selectivities are given on a carbon basis.

3. Results and discussion

3.1. Characterization of M@Al_2O_3 catalytic supports

3.1.1. Composition, structure, and texture of M@Al_2O_3 catalytic supports

Table 2 gives the experimental metal contents as well as the corresponding surface coverages (δ) for the MO_x oxidic species in the M@Al_2O_3 catalytic supports. As observed, the experimental surface coverages agreed well (relative deviations < 15%) with the nominal ones (Table 1).

Fig. 1 shows the X-ray diffractograms for the series of M@Al_2O_3 supports, along with that of the pristine γ-Al_2O_3 carrier. No diffractions apart from those corresponding to the alumina developed after the incorporation of the oxide promoters. A decrease in the intensity of the γ-Al_2O_3 diffraction signals was, however, noticed due to the dilution effect caused by the MO_x species, especially for Ta and lanthanide-bearing supports, for which high metal loadings (>15 wt.%) were needed to reach the monolayer coverage. The fact that no diffractions ascribed to MO_x species were detected implies that the oxidic promoters were present as amorphous phases or as very small crystallites (<2 nm), as expected for a two-dimen-

Table 2
Chemical composition and textural and electronic properties of $M@Al_2O_3$ catalytic supports.

Sample	Chemical composition		Textural properties (N_2-adsorption)				Electronic properties
	M (wt.%)	δ (M/nm^2)[a]	$S_{B.E.T.}$ (m^2/g)	PV[b] (cm^3/g)	PD[c] (nm)	PV[d] (cm^3/g Al_2O_3)	E(IMCT) (eV)[g]
Al_2O_3	–	–	205	0.51	8.9	0.52	–
$Fe@Al_2O_3$	7.9	4.7	169	0.43	8.5	0.48	(2.54[h]) 2.29[i]
$Ti@Al_2O_3$	6.8	4.7	193	0.44	7.5	0.47	2.51
$V@Al_2O_3$	10.3	6.9	179	0.38	7.3	0.47	(2.64[h]) 2.53[i]
$Nb@Al_2O_3$	15.1	5.9	185	0.38	7.2	0.49	2.59
$Ta@Al_2O_3$	23.5	5.2	176	0.34	7.0	0.48	2.52
$Y@Al_2O_3$	12.1[e]	4.6[e]	174	0.44	7.9	0.48	2.46
$Pr@Al_2O_3$	17.0[e]	4.4[e]	165	0.45	7.9	0.50	2.42
$Nd@Al_2O_3$	n.d.[f]	n.d.	159	0.42	7.8	n.d.	2.41
$Sm@Al_2O_3$	n.d.	n.d.	155	0.39	7.9	n.d.	2.38

[a] Surface coverage.
[b] Total pore volume.
[c] Mean pore diameter as determined by applying the B.J.H. formalism to the adsorption branch of the N_2 isotherm.
[d] PV corrected by the mass of MO_x. Bulk oxide stoichiometry has been assumed for MO_x.
[e] Chemical analysis for lanthanides has been carried out by XRF.
[f] n.d.: Not determined.
[g] Standard error ($s/N^{1/2}$) < 0.5% as determined from five independent measurements for $Sm@Al_2O_3$ and $Nb@Al_2O_3$.
[h] Determined for the as-calcined $M@Al_2O_3$ sample. In the case of basic promoters, the sample was previously decarbonated.
[i] Determined after a reduction treatment in flowing 10%H_2/N_2 at 750 K for $V@Al_2O_3$ and 850 K for $Fe@Al_2O_3$.

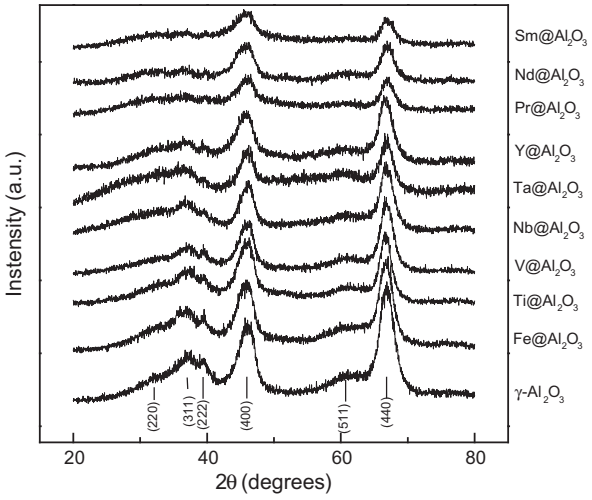

Fig. 1. X-ray diffraction patterns for the pristine Al_2O_3 carrier and the calcined $M@Al_2O_3$ catalytic supports. The diffraction lines for the γ-Al_2O_3 phase are indicated.

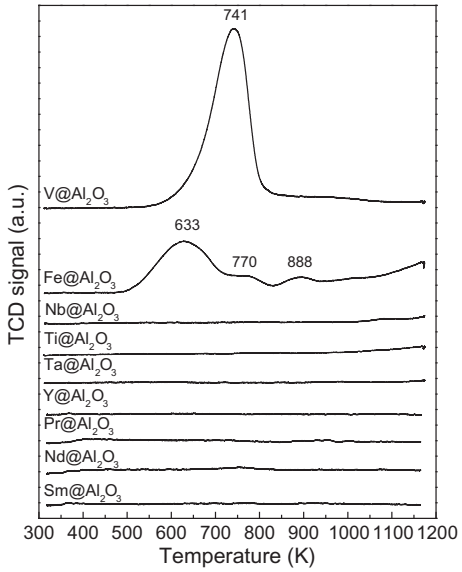

Fig. 2. H_2 TPR profiles for the $M@Al_2O_3$ catalytic supports.

sional arrangement of the oxide promoter on the alumina surface. Therefore, UV–vis spectroscopy was employed to characterize these XRD-silent MO_x species. As shown in Fig. S1 and Table S1 (Supplementary material), optical band gaps (E_g) in the range of 2.55–5.68 eV were obtained for the $M@Al_2O_3$ catalytic supports. The fact that these E_g values were systematically higher (by 0.25–1.15 eV) than those obtained for the corresponding bulk oxides (Table S1) confirmed the absence of XRD-undetectable MO_x bulk-like crystallites [43]. Thus, both XRD and UV–vis spectroscopy pointed to the achievement of a monolayer-like dispersion of amorphous MO_x species on the alumina surface.

The textural properties for the series of $M@Al_2O_3$ supports derived from the N_2 physisorption measurements are shown in Table 2. As seen there, the B.E.T. surface area, pore volume (PV), and mean pore diameter (PD) decreased compared to the pristine γ-Al_2O_3 carrier by 10–24%, 11–33%, and 4.5–21%, respectively, upon the incorporation of MO_x species. Nevertheless, the drop in surface area and PV can be attributed mainly to a mass-dilution effect caused by the MO_x phase. Indeed, when the PV is expressed per mass of Al_2O_3, the relative decrease with respect to the original γ-Al_2O_3 is below 9.7%, which nicely concurs with the expected volume occupied by the loaded MO_x species. This fact discards any extensive pore plugging by the loaded promoters.

3.1.2. Reducibility of promoters in $M@Al_2O_3$ catalytic supports

Fig. 2 shows the H_2 TPR profiles for the whole series of $M@Al_2O_3$ catalytic supports. As observed, supports bearing oxides of lanthanides (Pr, Nd, Sm), as well as those for Y, Ti, Ta, and Nb, did not show any discernible reduction feature in the temperature range 303–1173 K. In contrast, $Fe@Al_2O_3$ displayed several broad reduction signals in the range 523–973 K, while $V@Al_2O_3$ showed a unique intense reduction feature at 741 K. The reduction behavior of the MO_x promoters in the calcined solids, as well as the oxidation state of the MO_x promoters after the activation of $Rh/M@Al_2O_3$ catalysts, will be analyzed in Section 3.2.1.

3.1.3. Electronic properties of promoters in M@Al_2O_3 catalytic supports

Promotion mechanisms have been commonly suggested to involve electronic transfer between promoter and promoted catalytic phases, leading to different adsorption properties on the latter or to the creation of new hybrid catalytic sites at the promoter–active phase boundary [44]. It hence seems essential to study the electronic properties of the MO_x promoters in order to tackle promotion effects in Rh-based catalysts properly. Several universal scales for the electronic properties of metal oxides have been generated so far on the basis of descriptors such as the cation Sanderson electronegativity (S_M) [45], the cation and anion electronic polarizabilities (α_M, $\alpha_{O^{2-}}$) [46], the ionic–covalent parameter (ICP) [47], the optical band gap (E_g), or the optical basicity (Λ) [48].

In the present work, we have made use of DR UV–vis spectroscopy coupled to alizarine equilibrium adsorption to quantitatively rank the MO_x promoters according to their surface electron-withdrawing/donating power. This technique has been developed recently by Yoon and co-workers [38] and is based on the E(IMCT) from the cathecol moiety to the aromatic rings of the adsorbed alizarine, which has been recognized as a very sensitive probe for characterizing the surface electron-withdrawing/donating character (or Lewis acidity/basicity) for an extensive series of metal and lanthanide oxides [38]. Fig. 3a shows the UV–vis spectra for several alizarine surface-saturated supports, where the IMCT band for the adsorbed probe is apparent in the energy range 1.5–3.5 eV. A difference spectrum was required to ascertain the peaking energy for alizarine IMCT band when the MO_x species show d–d bands in this low-energy region, as for the partially reduced V@Al_2O_3 support (Fig. 3b). As shown in Table 2, E(IMCT) values in the range of 2.38–2.64 eV were obtained, the increase in E(IMCT) reflecting the increase in the acidic (electron-withdrawing) character of the M@Al_2O_3 catalytic support in its calcined form. In the case of the reducible V@Al_2O_3 and Fe@Al_2O_3 supports, the corresponding E(IMCT) values were significantly lowered after H_2 reduction (representative of their state prior to catalysis; see Section 3.2.1) in comparison with their calcined forms, which agrees with the expected decrease in Lewis acid character with the decrease in the oxidation state of the M cation [38]. Hence, as a conclusion of the present section, it could be stated that the series of MO_x promoters studied covered a wide range of electronic properties, going from oxides having a marked acidic (electron-withdrawing) character (VO_x, NbO_x, and TaO_x) to oxides displaying an obvious basic (electron-donating) character such as FeO_x (after reduction), PrO_x, NdO_x, and SmO_x, and oxides showing intermediate characteristics such as YO_x and TiO_x.

3.2. Characterization of model Rh/M@Al_2O_3 catalysts

3.2.1. Metal content, dispersion, and reducibility of Rh/M@Al_2O_3 catalysts

The Rh content in calcined Rh/M@Al_2O_3 catalysts determined by ICP-OES was in the range of 2.4–2.7 wt.%, corresponding to relative deviations <8% with respect to the nominal value of 2.5 wt.%.

The Rh metal dispersion in selected prereduced catalysts was assessed by means of CO chemisorption, TEM, and XPS.

Gas (H_2, CO) chemisorption is widely used to measure metal dispersion in catalysts. In the case of Rh/M@Al_2O_3 catalysts, M-dependent contributions from the MO_x species hampering a proper determination of the Rh^0 dispersion would be expected when H_2 was used as adsorbate, due to their capacity to store H-species spilt over from the Rh^0 crystallites [25,49]. In turn, CO chemisorption may be applied to determine Rh^0 dispersions as long as the actual CO/Rh_s surface stoichiometry is known. As seen in Table 3, CO uptakes of 286–349 μmol/g were found for selected reduced catalysts, corresponding to $CO/Rh_{(total)}$ molar ratios of 1.2–1.4. These high and relatively similar (standard deviation σ < 10% in $CO/Rh_{(total)}$ ratio) uptakes implied the absence of any M-dependent decoration or blockage of Rh^0 crystallites by the oxidic MO_x species in the as-reduced catalysts. However, the occurrence of several CO adsorption modes on the Rh crystallites (Section 3.4) does advise against a quantitative analysis of the CO chemisorption results in order to derive mean Rh NP sizes.

XPS-derived mean Rh^0 nanoparticle sizes for selected reduced catalysts are given in Table 3. As observed there, Rh nanoparticle sizes in the range of 2.0–2.6 nm were obtained for catalysts containing TaO_x, YO_x, and SmO_x as representative of the whole ranking established in Section 3.1.3. These results suggest homogeneity in the Rh dispersion within the series of catalysts, irrespective of the nature of the MO_x promoter on which the Rh is supported.

Additionally, TEM was employed to study metal dispersion in selected reduced catalysts. Fig. 4 shows representative TEM micrographs as well as the corresponding Rh NP size histograms for the reduced Rh/Ta@Al_2O_3, Rh/Y@Al_2O_3, and Rh/Sm@Al_2O_3 catalysts. In all cases, a narrow size distribution of small Rh nanoparticles (<3 nm) was observed, though the presence of very small (<0.5 nm) clusters or atomically dispersed Rh species, undetectable by high-resolution (HR) TEM, cannot be completely ruled out. As shown in Table 3, surface-averaged mean Rh nanoparticle sizes in the range of 1.0–1.3 nm were derived from TEM. Though there is a quantitative discrepancy in the mean $d(Rh^0)$ determined by TEM and XPS, most likely due to the assumptions inherent to the

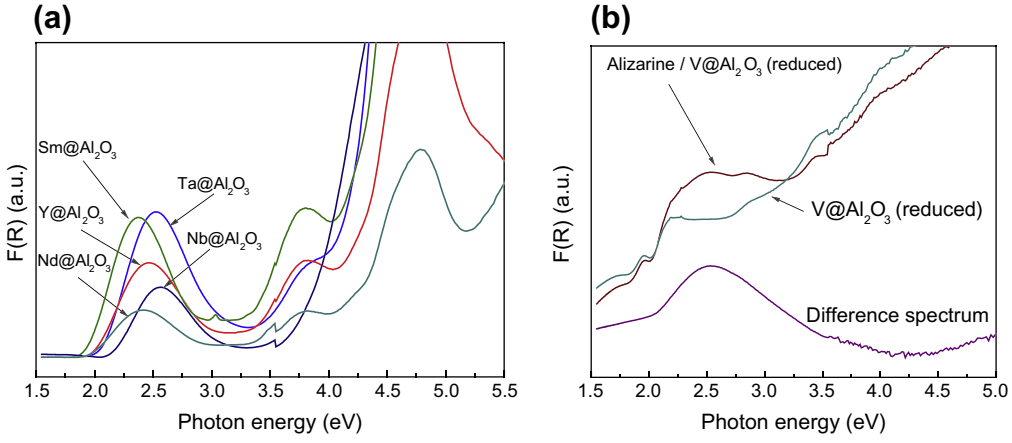

Fig. 3. (a) DR UV–vis spectra of selected calcined M@Al_2O_3 catalytic supports after saturation adsorption of alizarine; (b) DR UV–vis spectra for reduced (10%H_2/N_2, 750 K, 3 h) V@Al_2O_3 before and after saturation adsorption of alizarine, as well as the corresponding difference spectrum showing the IMCT band for the adsorbate.

Table 3
XPS, CO chemisorption, and TEM characterization results for selected Rh/M@Al_2O_3 catalysts.

Catalyst	State	XPS				CO chemisorption		TEM	
		M[a] BE (eV)	Rh3$d_{5/2}$ BE[b] (eV)	%[c]	d(Rh)[d] (nm)	CO uptake[e] (μmol/g)	CO/Rh[f]	d(Rh)[g] (nm)	σ[h] (nm)
Rh/V@Al_2O_3	Calcined	517.6 (V^{5+})	310.1 ($RhCl_3$)	100	–	–	–	–	–
Rh/V@Al_2O_3	Reduced	515.9 (V^{3+})	307.3 (Rh^0)	90	–	–	–	–	–
			310.4 ($RhCl_3$)	10					
Rh/Ta@Al_2O_3	Reduced	230.1 (Ta^{5+})	306.9 (Rh^0)	88 (89)	2.6	286	1.2	1.1	0.3
			310.1 ($RhCl_3$)	12 (11)					
Rh/Y@Al_2O_3	Calcined	158.2 (Y^{3+})	309.4 (Rh_2O_3)	100	–	–	–	–	–
Rh/Y@Al_2O_3	Reduced	158.3 (Y^{3+})	307.1 (Rh^0)	100	2.1	349	1.4	1.3	0.3
Rh/Sm@Al_2O_3	Reduced	1083.8 (Sm^{3+})	306.8 (Rh^0)	83 (81)	2.0	321	1.2	1.1	0.3
			308.9 (Rh_2O_3)	17 (19)					

[a] Binding energy for the 2p line of V and the 3d line of the remaining promoters (M).
[b] Binding energy for the Rh3$d_{5/2}$ line.
[c] Relative contribution of each species (%). Values in parentheses correspond to the sample after in situ treatment under syngas flow at 553 K for 2.5 h.
[d] Mean Rh nanoparticle size as estimated from quantitatively interpreting the XPS spectra for reduced catalysts employing the Kerkhof–Moulijn model (see text for details).
[e] Irreversibly chemisorbed CO uptake.
[f] Ratio of CO molecules to total Rh atoms.
[g] Surface-averaged Rh nanoparticle size, as determined from TEM measurements, $d(Rh) = \frac{\sum_i n_i \cdot (d_i)^3}{\sum_i n_i \cdot (d_i)^2}$. Between 100 and 150 measurements at different micrographs were used to obtain size histograms.
[h] Standard deviation for the Rh nanoparticle size distributions, as determined from TEM measurements.

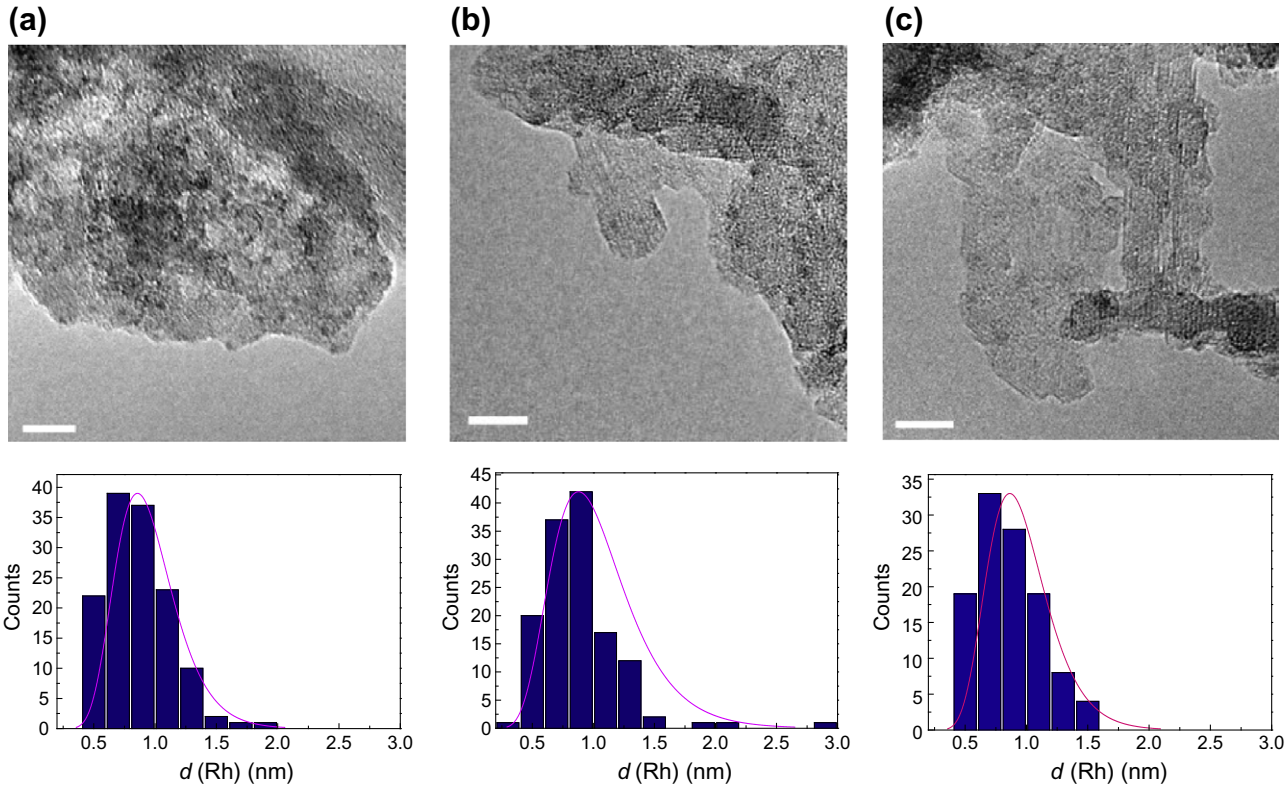

Fig. 4. Representative TEM micrographs and the corresponding Rh particle size histograms (including lognormal fit) for H_2 reduced (a) Rh/Ta@Al_2O_3, (b) Rh/Y@Al_2O_3, and (c) Rh/Sm@Al_2O_3 catalysts. Scale bar: 5 nm.

model applied for the quantitative interpretation of the XPS data (see Section 2.2), the results derived from both techniques are in favor of a high and homogenous metal dispersion within the series of Rh model catalysts, likely as a result of the homogeneous textural properties of the M@Al_2O_3 supports. These features made the present set of catalysts ideal to study Rh promotion without overlap from metal NP-size related effects.

Besides metal dispersion, the reduction behavior of both MO_x promoters and Rh species seems also of paramount importance for catalysis, since it might strongly determine their adsorption and electronic properties. Fig. 5 shows the H_2 TPR profiles for selected Rh/M@Al_2O_3 catalysts. As observed, all catalysts displayed a single reduction signal at rather low temperatures (383–443 K), which, in principle, should be related to the reduction of cationic Rh species to Rh^0. It is worth to notice, however, that the high-temperature (523–973 K) reduction features observed for FeO_x and VO_x in the Rh-free catalytic supports (Fig. 2) were not longer present in the profiles of the corresponding Rh/M@Al_2O_3 catalysts. This fact suggests that the reductions related to the FeO_x and VO_x phases shifted to much lower temperatures in the presence of Rh, contributing, together with the reduction of Rh species, to the single low-temperature reduction signal at $T < 423$ K. Such a Rh-assisted

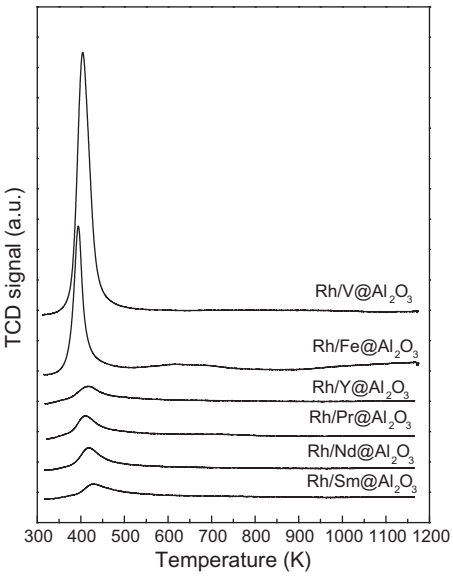

Fig. 5. H_2 TPR profiles for selected Rh/M@Al_2O_3 catalysts.

reduction of FeO_x and VO_x phases likely involves H_2 dissociation on the forming Rh^0 sites and migration through a spillover mechanism to the neighboring MO_x species, promoting their co-reduction.

Indeed, a quantitative analysis of the H_2 consumptions for the M@Al_2O_3 supports and the corresponding Rh/M@Al_2O_3 catalysts confirmed that the reduction of FeO_x and VO_x promoters took place along with that of Rh species at $T < 423$ K and to the same extent as at much higher temperatures in the bare catalytic supports. The analysis also revealed the lack of significant reductions for the remainder of nonreducible promoters in the presence of Rh. Thus, the series of MO_x promoters comprised both reducible oxides such as FeO_x and VO_x, which will be partially reduced after the H_2 reductive pretreatment applied prior to catalysis (573 K), and oxides that will not be appreciably reduced under these conditions and thus will remain in the same oxidation state after H_2 reduction as in their calcined form.

3.2.2. Oxidation state and electronic properties of Rh NPs in reduced Rh/M@Al_2O_3 catalysts

A series of selected catalysts were studied by XPS to gather information on the oxidation states of promoters and Rh, as well as on the electronic properties of the supported Rh NPs, after the same reductive treatment applied prior to catalysis. The Rh3*d* XPS spectra for the in situ H_2 reduced selected catalysts are shown in Fig. S2 (Supplementary material). Additionally, Table 3 gives the quantitative results derived from this XPS study.

With regard to the MO_x promoter species, TaO_x-, YO_x-, and SmO_x-promoted catalysts exhibited exclusively Ta^{5+} ($BE_{Ta4d_{5/2}}$ = 230.1 eV), Y^{3+} ($BE_{Y3d5/2}$ = 158.3 eV), and Sm^{3+} ($BE_{Sm3d_{5/2}}$ = 1083.8 eV) after reduction (Table 3), evidencing the absence of any reduction for these promoter oxides during the hydrogen pretreatment. Conversely, Rh/V@Al_2O_3 displayed uniquely V^{5+} ($BE_{V2p_{3/2}}$ = 517.6 eV) species in its calcined form, but exclusively V^{3+} ($BE_{V2p_{3/2}}$ = 515.9 eV) after H_2 reduction, confirming the partial reduction of the VO_x promoter in this case. Thus, these results validate the discussion of H_2 TPR characterization in Section 3.2.1.

Regarding the Rh species, $RhCl_3$ ($BE_{Rh3d_{5/2}}$ = 310.2 ± 0.2 eV) was the unique Rh species detected in VO_x- (Table 3) and TaO_x-promoted (not shown) catalysts in their calcined states, whereas it was present as Rh_2O_3 ($BE_{Rh3d_{5/2}}$ = 309.2 ± 0.2 eV) [50] in calcined YO_x- (Table 3) and SmO_x-promoted (not shown) catalysts. This fact suggests that the chlorinated Rh precursor is somehow stabilized on electron-withdrawing oxides. With regard to this, it is known that the metal atom in $RhCl_3$ is a Lewis acid, which might interact more strongly with the electron-donating (basic) oxides such as YO_x and SmO_x, promoting the decomposition of $RhCl_3$ during calcination.

After H_2 reduction (573 K, 6 h), Rh^0 ($BE_{Rh3d_{5/2}}$ = 306.8–307.3 eV) species predominated on the catalyst surface for all the studied samples, along with minor amounts (<17% in relative terms) of the remaining Rh_2O_3 ($BE_{Rh3d_{5/2}}$ = 308.7–309.5 eV) or $RhCl_3$ ($BE_{Rh3d_{5/2}}$ = 310.0–310.4 eV) species, depending on the nature of the Rh species existing in the corresponding calcined catalyst as discussed above.

XPS can also be used to gain insight into the electronic properties of the Rh^0 crystallites in the as-reduced catalysts. As shown in Table 3, Rh^0 BE values in the range of 307.0 ± 0.3 eV were obtained for the several analyzed catalysts. The XPS BE is a very complex parameter, since it includes both initial state and final state effects. Due to the complexity of this parameter, some authors have considered the modified Auger parameter in order to determine initial state effects. However, the low peak intensity of the Rh M5VV Auger transition in our samples (not shown) made the estimation of the Auger parameter tricky. Considering only BE values, no obvious variation in the electronic properties for the supported Rh^0 crystallites within the series of Rh/M@Al_2O_3 catalysts was inferred.

Besides, in order to study possible changes in the oxidation state of the Rh^0 NPs under reaction conditions (at atmospheric pressure), in situ XPS experiments were performed for selected catalysts. As shown in Table 3, no significant changes in the relative proportion of metallic and oxidized Rh species (thus in the oxidation state of the supported Rh NPs) with respect to the corresponding as-reduced samples were noticed for Rh/Ta@Al_2O_3 and Rh/Sm@Al_2O_3 catalysts upon exposure to syngas (atmospheric pressure, 553 K) for 2.5 h.

3.3. Catalytic properties of Rh/M@Al_2O_3 model catalysts in the SSO

Table 4 summarizes the catalytic results for the series of Rh/M@Al_2O_3 catalysts. As observed, a maximum in the Rh-time-yield (RTY) was attained for Rh/Fe@Al_2O_3, while catalysts promoted by transition metal oxides of groups 4 (Ti) and 5 (V, Nb, Ta) showed specific activities 2- to 2.5-fold lower. Also, catalysts promoted by Y and lanthanide oxides were the less active of the series, showing RTY values up to tenfold lower than that of the FeO_x-promoted catalyst. Considering the Rh NP sizes estimated by XPS (Table 3) and assuming a spherical NP geometry with a surface site density of 14.6 Rh/nm^2, these RTY values corresponded to *turnover frequencies* (TOF) ranging from 1.3×10^{-2} s^{-1} for Rh/Ta@Al_2O_3, as representative of the catalysts promoted by acidic oxides, to 1.8–3.2×10^{-3} s^{-1} for the less active YO_x- and SmO_x-promoted catalysts, illustrative of lanthanide oxide-promoted catalysts. A direct comparison of these site-activities with previous literature data is not straightforward, owing to the various reaction conditions employed (the reaction temperature being particularly influential) and the several techniques applied by different authors to measure metal dispersion. A value generally in the range of 80–100 kJ/mol has been found for the apparent activation energy (E_a) of CO hydrogenation on Rh catalysts. Particularly, E_a = 83 kJ/mol is derived from the results reported by Haider et al. [22]. Employing this E_a value, reported TOF values obtained at several reaction temperatures can be compared with those obtained for our model catalysts at 553 K, after translating to the corresponding TOF_{553} (at 553 K), by assuming an Arrhenius dependence of TOF with temperature. Upon doing so, TOF values in the range of 1–4 $\times 10^{-2}$ s^{-1} were obtained for Rh/TiO_2 [22], in fairly good agreement with those reported here for catalysts promoted by group 4 and group 5 metal

Table 4
Catalytic results for the SSO employing the Rh/M@Al_2O_3 catalysts under reaction conditions T = 553 K, P = 5.0 MPa, H_2/CO = 1, X_{CO} = 15 ± 3%.

Catalyst	RTY[a]	Selectivity (%C)					
		HC[b] (%)	CO_2 (%)	Oxyg.[c] (%)	Oxygenates fraction		ROH
					ROH[d] (%)	[AcOOH + AcOOR][e] (%)	$[C_{2+}/C_1]$[f]
Rh/Fe@Al_2O_3	4.28	51.4	7.5	41.1	86.2	8.6	3.2
Rh/V@Al_2O_3	1.93	70.1	7.0	23.0	54.5	38.4	5.2
Rh/Nb@Al_2O_3	1.69	78.7	9.3	12.0	41.4	50.4	1.5
Rh/Ta@Al_2O_3	2.10	75.5	4.1	20.4	46.0	51.5	2.8
Rh/Ti@Al_2O_3	1.65	70.3	3.2	26.5	41.2	54.0	2.5
Rh/Y@Al_2O_3	0.64	58.7	5.1	36.2	70.5	26.2	3.0
Rh/Pr@Al_2O_3	0.53	44.1	4.7	51.2	72.4	22.2	2.1
Rh/Nd@Al_2O_3	0.44	42.6	8.9	48.5	78.5	17.0	1.7
Rh/Sm@Al_2O_3	0.39	30.6	10.0	59.4	83.4	12.2	0.7
Rh/Li–Ta@Al_2O_3	2.20	64.0	4.1	31.9	34.8	59.9	2.0

[a] Pseudo-steady Rh-time-yield (10^{-1} mol_{CO} g_{Rh}^{-1} h^{-1}).
[b] HC: hydrocarbons.
[c] Oxyg.: oxygenated compounds.
[d] ROH: Alcohols.
[e] AcOOH + AcOOR: acetic acid + acetates.
[f] Higher alcohols-to-methanol ratio in the alcohols fraction.

oxides. Alternatively, Underwood and Bell [51] measured catalytic activities equivalent to TOF_{553} = 1.4–2.6 × 10^{-3} s^{-1} for Rh/Ln_2O_3 (*Ln* = La, Nd, Sm), in line with the site-activity reported here for the model catalysts based on lanthanide oxides. Then, it is concluded from these comparisons that the model Rh/M@Al_2O_3 catalysts studied here show intrinsic catalytic activities coherent with those previously reported for Rh NPs supported on the corresponding bulk oxides. On the other hand, higher TOF values were found for SiO_2-supported Rh NPs containing a small amount (<3 wt.%) of metal oxides as promoters. Thus, TOF_{553} of 6 × 10^{-2} s^{-1} and 1.2 × 10^{-1} s^{-1} are derived from previous studies employing Rh–LaO_x–VO_x/SiO_2 [13,52] and Rh–MnO_x–LiO_x–FeO_x/SiO_2 [53] catalysts, respectively. Even though it appears from the comparison that SiO_2-supported Rh catalysts might be intrinsically more active than our model systems, other effects related to differences in the Rh NP size or to the reaction conditions cannot be ruled out. In this respect, a threefold increase in TOF has been reported to occur when the H_2/CO ratio is increased from 1 (employed in this work) to 2 (typically applied to Rh–MO_x/SiO_2 catalysts) [22].

Besides the notable differences in catalytic activity observed in this study depending on the nature of the MO_x promoter, significant variations in the selectivity pattern (at constant CO conversion of ca. 15%) were also evidenced. Thus, while catalysts promoted by FeO_x and lanthanide oxides (PrO_x, NdO_x, SmO_x) displayed the highest oxygenate selectivity (41.1–59.4%) with a predominance of alcohols within this fraction (>70%), those promoted by oxides of group 4 and 5 transition metals produced hydrocarbons as the major reaction products (>70% selectivity). Moreover, in the case of TiO_x-, NbO_x-, and TaO_x-promoted catalysts, carboxylic compounds (mostly acetic acid and methyl and ethyl acetates) were the main products (>50% selectivity) within the oxygenate fraction. These results suggest important differences in the nature and proportion of active sites depending on the particular promoter oxide, which determine the relative importance of several reaction pathways during the SSO process.

As already mentioned with respect to TOF, comparing the selectivities obtained for our model catalysts with those previously published for related systems might be tricky, owing to the wide range of experimental conditions employed in different works. Nonetheless, selectivities to hydrocarbons and oxygenates of ca. 60–80% and 20–40% (C basis), respectively, have been reported for Rh–VO_x/SiO_2 [13] and Rh/TiO_2 catalysts [22]. These results are consistent with the selectivities obtained here for catalysts promoted by group 4 and 5 metal oxides. Furthermore, the addition of La_2O_3 to a Rh–VO_x/SiO_2 catalyst was seen to improve the selectivity to oxygenates [13], which is in line with the higher oxygenate selectivity afforded by the model catalysts promoted by lanthanide oxides in our study. Thus, the trends observed for our model Rh/M@Al_2O_3 catalysts might be helpful in predicting/understanding the catalytic behavior for alternative catalytic systems. Nevertheless, it should be pointed out that selectivities to ethanol significantly higher (ca. 50% on a carbon basis [54]) than those obtained in the present study have been reported for SiO_2-supported promoted Rh catalysts with optimized composition under suitable reaction conditions.

The widely accepted reaction pathway [14,55] leading to hydrocarbons initially involves the dissociation of H_2 and CO (the later might be H-assisted) and the formation of partially hydrogenated C_xH_y species that may undergo chain-growing events before being desorbed through hydrogenation (paraffins) or β-hydrogen abstraction (α-olefins), following a Fischer–Tropsch-like mechanism. These nonoxygenated adsorbed C_xH_y species may also take part in the reaction pathways to higher (C_{2+}) oxygenates, for which a catalytic event involving the chain-insertion of a nondissociated CO molecule precedes the product desorption. Finally, C_1 oxygenates are generally believed to derive from the direct hydrogenation of nondissociatively activated CO molecules [56,57].

The great variety of reaction products displaying different chain lengths and bearing or not bearing oxygenated functional groups certainly complicates the discussion of the *promotion effect* for this catalytic system. All the previously published scientific work on Rh-catalyzed SSO merely considered the relative selectivities to oxygenates, certain families of oxygenates, or specific compounds in their discussions. The present study attempts to take a step forward and, profiting from the wide variety of selectivity patterns obtained for our model Rh/M@Al_2O_3 catalysts, consider the implications of the CO dissociation/insertion balance for the product nature and chain length in a more quantitative way.

For this purpose, a *selectivity descriptor* ($\Phi = C_{ins}/C_{dis}$) is defined here to ponder the presence of two kinds of C atoms in the reaction products: those arising from CO dissociation (C_{dis}) and those coming from nondissociative CO insertion (C_{ins}), according to the accepted reaction pathways already discussed [14,55]. The first type of carbon atoms (C_{dis}) are the only ones present in hydrocarbons but also appear in C_{2+} oxygenates and derive from intermediate C_xH_y species. In contrast, C_{ins}-type carbon atoms appear bonded to oxygen atoms in C_{2+} oxygenates and are the only ones in C_1

oxygenates and dimethyl ether. In order to quantify C_{dis} and C_{ins} in the reaction products, ethers were considered as derived from the two corresponding alcohols through secondary dehydration events. Thus, by its own definition, Φ represents the balance between the capacity to insert nondissociated CO molecules into the reaction products and to dissociatively activate CO.

Fig. 6 illustrates the evolution of the selectivity parameter (Φ) against the electronic properties of the promoter species (MO_x) described by the E(IMCT) values of adsorbed alizarine. As observed, a potential-like correlation between Φ (in the range of 0.08–0.94) and E(IMCT) (in the range of 2.38–2.59 eV) was found, according to which the proportion of C_{ins} in the reaction products progressively increases (i.e., Φ increases) when the electron-donating character (or Lewis basicity) of the promoter species is increased. This correlation involved all catalysts bearing nonreducible MO_x promoters, that is, those that did not undergo reduction during the H_2-reduction pretreatment and whose E(IMCT) in the calcined state was representative of their properties after the H_2-activation. However, the picture looked different for the two catalysts bearing reducible promoters ($Rh/Fe@Al_2O_3$ and $Rh/V@Al_2O_3$). As observed in Fig. 6, a significant deviation from the general correlation shown by the guideline was apparent for these two catalysts when the E(IMCT) values obtained in their oxidized form (open symbols) were considered. In the case of $Rh/V@Al_2O_3$, however, considering the E(IMCT) value obtained after the proper H_2-activation (closed symbol in Fig. 6) appeared essential to incorporate this catalyst into the general trend, thus pointing to the need to characterize the electronic properties of the reducible promoters in their reduced state, to which they are set after the H_2-reduction treatment prior to catalysis. Conversely, a significant deviation from the general correlation was apparent for the FeO_x-promoted catalyst in both its calcined and reduced states, which suggests that the promoting mechanism for FeO_x cannot be described using the E(IMCT) descriptor, as for the rest of the oxidic promoters. Probably, the much higher catalytic activity displayed by this catalyst (Table 4) is also related to this fact. A priori, the main difference between supported iron oxide and the rest of the promoters, which might be behind the out-of-trend behavior of $Rh/Fe@Al_2O_3$, is its known capability to undergo carbidization and then activate both CO and H_2 under the reaction conditions employed for the SSO, being indeed a catalyst of choice for the Fischer–Tropsch synthesis [58]. The formation of Fe–Rh alloys, already claimed to form on similar

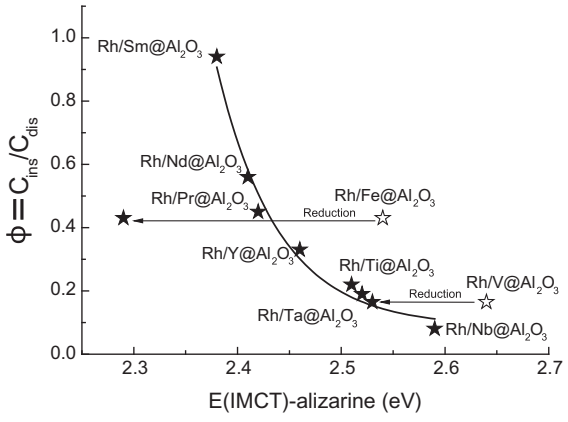

Fig. 6. Evolution of the selectivity parameter (Φ) with the electronic properties of the MO_x promoter phase using the E(IMCT) for adsorbed alizarine as descriptor. Open symbols correspond to the characterization of $Fe@Al_2O_3$ and $V@Al_2O_3$ supports in their as-calcined state and closed symbols correspond to the characterization of promoter species in the oxidation state representative for the catalytic state, i.e., prereduced for FeO_x and VO_x and as-calcined for the remaining nonreducible MO_x.

$Ir–FeO_x/SiO_2$ systems under syngas conversion conditions [59], might also be contemplated. These specific features might provide alternative reaction pathways in the SSO conditions. The general approach employed in the present study seems not to be valid for the case of using FeO_x as an Rh promoter, and this particular system would require future insights following alternative considerations and further characterizations.

It is worth mentioning here that an additional factor such as the intramolecular dehydration of alcohols to olefins could, in principle, contribute to the value of Φ, and thus to the trend depicted in Fig. 6. This acid-catalyzed secondary reaction would result in an underestimation of Φ as, formally, C_{ins}-bearing products are converted into purely C_{dis} products plus water. Considering that Al_2O_3-supported group 5 metal oxides might contain Brønsted and Lewis acid sites [29], and that some acid sites could also be exposed on uncovered regions of the alumina surface, it was pertinent to determine whether they contributed or not to catalyzing intramolecular alcohol dehydration reactions and thus to the obtained correlation. With regard to this, there is certain experimental evidence that does favor a negligible contribution of secondary intramolecular alcohol dehydration to the calculated Φ values. On one hand, as is shown in Fig. S3 (Supplementary material), the hydrocarbon fraction obtained with the acidic NbO_x- and TaO_x-promoted catalysts nicely followed the typical Anderson–Schulz–Flory (ASF) distribution, suggesting that these products were predominantly formed through a Fischer–Tropsch-like polymerization mechanism and, hence, with negligible (if any) contribution from alcohol dehydration reactions. On the other hand, acid-site titration did not lead to a marked increase in alcohol production. In this respect, it is known that at monolayer coverage, Al_2O_3-supported 2D VO_x, NbO_x, and TaO_x bear around 0.7–0.8 (Brønsted + Lewis) acidic sites/nm^2 [29]. Alkaline metals (Na, Li, K) have been widely applied to neutralize the acidity in SSO catalysts [60], the use of Li being particularly common in Rh-based systems [53,61]. Hence, to probe the acid-site titration approach, a $Rh/Li–Ta@Al_2O_3$ catalyst containing 1.0 Li/nm^2 (20–30% in excess with respect to the expected acid-site density) was prepared as detailed in Section 2. As shown in Table 4, the addition of Li slightly reduced the selectivity to hydrocarbons in favor of oxygenates, but hardly modified the ASF distribution for the former (Fig. S3). Consequently, neutralizing the surface acidity through the addition of Li led to a limited increase in Φ from 0.19 ($Rh/Ta@Al_2O_3$) to 0.29 ($Rh/Li–Ta@Al_2O_3$), which barely modified the correlation depicted in Fig. 6. Thus, it can be concluded that the formation of hydrocarbons most likely takes place through a Fischer–Tropsch-like mechanism on metallic sites and that secondary acid-catalyzed reactions do not contribute substantially to the trends discussed under the reaction conditions employed.

In line with this conclusion, some previous results can be revised here. Ichikawa et al. [10,11], working under atmospheric pressure (thus favoring low chain-growth probabilities), found a significant formation of methane (which obviously cannot derive from secondary alcohol dehydrations) in Rh catalysts supported on acidic bulk oxides such as SiO_2, Al_2O_3, SnO_2, V_2O_5, or WO_3. Interestingly, the same authors concluded that middle alkaline or so-called amphoteric supports such as TiO_2, ZrO_2, or La_2O_3 maximized C_{2+} oxygenates, while more basic oxides (MgO, CaO, BeO) promoted the formation of methanol, which can be seen as an antecedent for the trends studied, for the first time quantitatively, in the present work.

An additional aspect to be considered regarding the influence of the electronic properties of the promoters on the selectivity pattern is that Φ (C_{ins}/C_{dis}) is not exclusively related to the hydrocarbons-to-oxygenates ratio but, by its own definition, should also be associated with the mean chain length of the formed products (both hydrocarbons and oxygenates), since growing C_xH_y chains

have C atoms derived from CO dissociation. In this sense, C_{2+} alcohols are highly desired reaction products, and thus maximizing their production against methanol constitutes a target in the SSO. As shown in Fig. 7, there was a fine linear correlation between the C_{2+}/C_1 ratio in the alcohol fraction and the *E*(IMCT) value for the series of catalysts promoted by YO_x, PrO_x, NdO_x, and SmO_x, which showed, besides $Rh/Fe@Al_2O_3$, the highest selectivity to alcohols. This correlation confirmed the dependence of the mean chain-growth probability for alcohols on the nature of the MO_x promoter, as described by the *E*(IMCT) parameter. This dependence of the alcohols' mean chain length as a function of the electronic properties of the MO_x promoters leads to important variations in the relative contribution of higher (C_{2+}) alcohols in this product fraction, varying from 75% for $Rh/Y@Al_2O_3$ to only 33% for $Rh/Sm@Al_2O_3$.

Finally, with regard to the catalytic activity, a direct relationship between the rhodium-time-yield (RTY) and the selectivity pattern (described by Φ) was evidenced, as shown in Fig. S4 of the Supplementary material, according to which RTY decreased as the proportion of C_{ins} in the products increased. Thus, the specific CO conversion rate is just a consequence of the balance between the two CO activation mechanisms (C_{dis} vs. C_{ins}), suggesting that the rate-determining step (RDS) for the reaction pathway involving CO dissociation is faster than the corresponding RDS for the non-dissociative CO insertion pathway.

As a summary of the present section, it can be stated that the electronic properties (electron-withdrawing/donating power or Lewis acidity/basicity) of the oxidic promoters exert control on both the catalytic activity and the selectivity of Rh catalysts during the SSO, according to which more basic (electron-donating) promoters lead to intrinsically less active and more oxygenate-selective catalysts by favoring the nondissociative CO insertion pathway, whereas acidic (electron-withdrawing) promoters show both higher specific activity and hydrocarbon selectivity by facilitating CO dissociation events. In principle, these promotions should act through certain electronic and/or geometric effects exerted on the supported Rh NPs and/or by creating new active sites at the Rh–MO_x boundary. According to the XPS results previously discussed, no evident changes in the electronic properties of the supported Rh NPs with the nature of the underlying MO_x promoter were found. However, the possible influence of the electronic character of the MO_x promoter on the Rh particle morphology and/or on the nature of the adsorption sites at the metal–support interface is not discernible by XPS and, thus, the use of more surface-sensitive techniques such as IR spectroscopy coupled with the adsorption of highly sensitive probe molecules (i.e., CO) is advised. For this reason, a study of the interaction of Rh NPs with CO using low-temperature and at-work CO-FTIR was undertaken here in order to gain insight into promotion effects in selected MO_x-promoted catalysts.

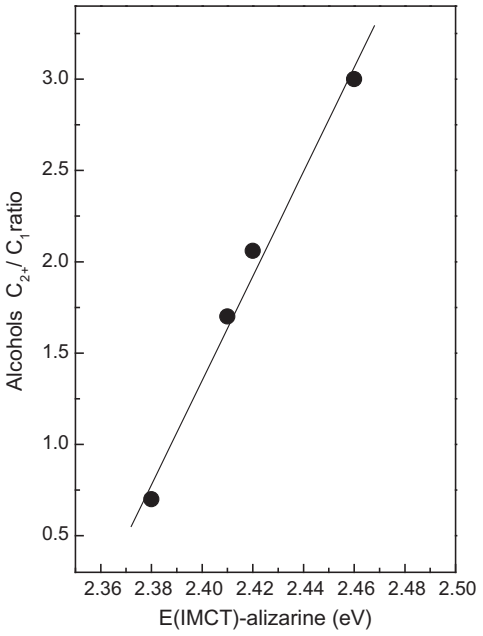

Fig. 7. Evolution of the C_{2+}/C_1 ratio in the alcohols product fraction for lanthanide oxide-promoted $Rh/M@Al_2O_3$ catalysts as a function of the electronic properties of the promoter oxides as described by the *E*(IMCT) of adsorbed alizarine.

3.4. CO-FTIR investigation into the interaction of Rh NPs with CO

3.4.1. Adsorption of CO at low temperature

Low-temperature CO-FTIR is known to be a powerful technique for studying surface topology and partial electronic charges on surface metal atoms. Figs. 8 and 9 show, respectively, the CO-FTIR spectra at 77 K for the in situ reduced $Rh/Sm@Al_2O_3$ and $Rh/Ta@Al_2O_3$ catalysts as representative of the two extreme behaviors of the trend depicted in Fig. 6. In both cases, bands in the region of 2200–1220 cm^{-1} were observed. In this spectral region, IR bands due to Rh carbonyls (IR bands at 2100–1770 cm^{-1}) and to M^{n+} carbonyl

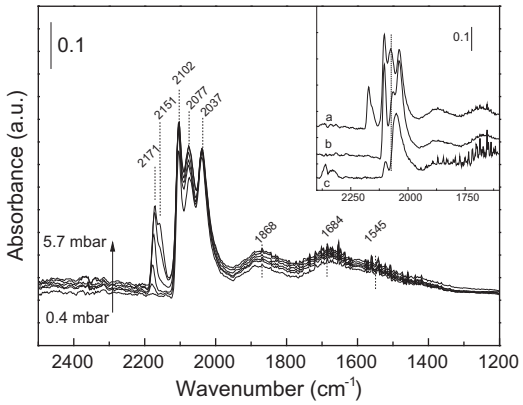

Fig. 8. CO-FTIR spectra after several CO doses (0.4–5.7 mbar) at 77 K on the in situ reduced (H_2, 573 K) $Rh/Sm@Al_2O_3$ catalyst. The inset shows the spectra at 5.7 mbar CO (a) and after dynamic evacuation (<10^{-4} mbar) for 1 min at 193 K (b) and for 10 h at RT (c).

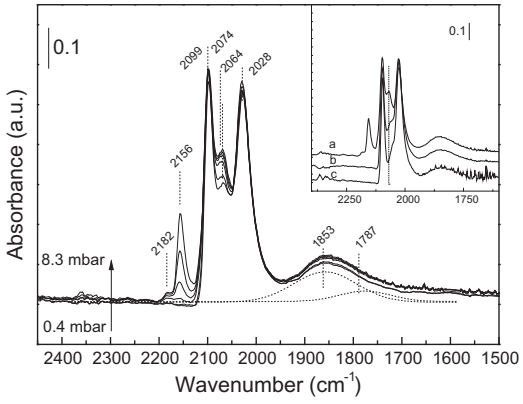

Fig. 9. CO-FTIR spectra after several CO doses (0.4–8.3 mbar) at 77 K on the reduced (H_2, 573 K) $Rh/Ta@Al_2O_3$ catalyst. The inset shows the spectra at 8.3 mbar CO (a) and after dynamic evacuation (<10^{-4} mbar) for 1 min at 193 K (b) and for 10 h at RT (c).

species associated with Lewis acid sites and/or OH groups of the oxide species (IR bands at 2180–2150 cm^{-1}) were evidenced. According to the change observed in the IR region of the hydroxyl groups after CO adsorption, small amounts of acid OH groups were observed in the $Rh/Ta@Al_2O_3$ sample (IR bands at 2156 and 2182 cm^{-1}, Fig. 9), while they were not detected in the $Rh/Sm@Al_2O_3$ sample. In the last case, the IR bands at 2171 and 2151 cm^{-1} (Fig. 8) are related to surface Lewis acid sites of the promoter. In the Rh carbonyls ($Rh(CO)_x$) region, intense bands at ca. 2100 and 2030 cm^{-1}, associated respectively with the ν_s and ν_a vibrations of *gem*-dicarbonyl species ($Rh^I(CO)_2$), along with weaker bands at 2060–2080 cm^{-1} ascribed to CO linearly adsorbed onto Rh^0 ($Rh^0(CO)_L$) and a broader signal at ca. 1860 cm^{-1} arising from CO adsorption onto Rh^0 in a bridged configuration ($Rh_2(CO)_B$) [26] were evidenced. Additionally, in the case of $Rh/Sm@Al_2O_3$ (Fig. 8), weak bands were observed at 1684 and 1545 cm^{-1}, which can be ascribed to the formation of surface carbonates on the basic SmO_x oxide upon exposure to CO. On the other hand, a band at 1787 cm^{-1} was observed in the spectrum of $Rh/Ta@Al_2O_3$ (Fig. 9), which, according to previous works, might be ascribed to the tilted adsorption mode of CO at the Rh–MO_x boundary [62–64]. The generally assumed structure for this adsorption mode consists of the C atom binding to a metallic Rh site and the electron-richer O atom stabilized on a neighbor electropositive M atom.

Deconvolution of the IR spectra for these two samples (not shown) indicated a higher dicarbonyls-to-monocarbonyls band intensity ratio for the TaO_x-promoted catalyst than for that promoted by SmO_x, pointing toward a higher surface fraction of partially oxidized Rh(I) species in the former. Additionally, the evacuation spectra (see insets in Figs. 8 and 9) pointed to higher stability of the dicarbonyl species in the case of $Rh/Ta@Al_2O_3$, for which the IR signals ascribed to $Rh^I(CO)_2$ were not significantly modified by prolonged outgassing. In contrast, the dicarbonyl bands in $Rh/Sm@Al_2O_3$ were almost suppressed upon outgassing.

Moreover, different frequencies for the monocarbonyl IR bands were observed for SmO_x- and TaO_x-promoted samples, indicating the presence of various Rh surface species showing a distinct electron back-donation to the antibonding CO molecular orbital. Specifically, IR bands at 2074 and 2064 cm^{-1} were observed for the TaO_x-promoted catalyst (Fig. 9), while a band at 2077 cm^{-1} was observed for the SmO_x-promoted sample (Fig. 8). On both $Rh/Sm@Al_2O_3$ and $Rh/Ta@Al_2O_3$ samples, the $Rh^0(CO)_L$ IR band shifted to lower frequency (shift of ca. 9 and 17 cm^{-1}, respectively) upon evacuation, due to decreased dipole–dipole interaction (insets in Figs. 8 and 9).

More remarkably, the intensity ratio for the linear and bridged carbonyl bands (L/B ratio) was significantly different for these two catalysts. Thus, bridged CO carbonyls exhibited a considerably higher relative intensity in the TaO_x-promoted sample (L/B = 0.8) than in that promoted by SmO_x (L/B = 2.6). The L/B ratio has been proposed to be directly related to geometric factors such as metal crystallite size and/or morphology, determining the relative exposure of different metal facets, as well as to electronic effects, namely the partial electronic charge on metal NPs [65,66]. XPS and HRTEM results evidenced marginal variations in Rh^0 NP size within the series of model catalysts in their reduced state (Table 3), and hence, size effects cannot account for the differences ascertained by CO-FTIR on the examined as-reduced catalysts. The same holds true for the partial electronic charge, since, according to XPS results, there were no significant variations in the mean electronic density for Rh^0 nanocrystals within the series of catalysts studied. Thus, it appears reasonable to hypothesize that morphological differences in the supported Rh NPs might be behind the distinct CO adsorption properties for Rh^0 crystallites supported on either TaO_x or SmO_x. Raft-like metal NPs are known to promote bridged adsorption of CO on planar facets, as compared to more rugged 3D NPs, which display higher L/B ratios [66]. In consequence, it seems pertinent to infer a more planar morphology for the Rh crystallites supported on the TaO_x species. Indeed, in line with the present results, the morphology adopted by very small metal NPs (<3 nm) in supported catalysts has been related previously to the electronic nature of the underlying support [66,67]. However, metal nanoparticle size/shape in the as-reduced catalysts might be modified by exposure to reactants and products under catalysis conditions. Thus, the following section extends the CO-FTIR study to reaction conditions under syngas flow at atmospheric pressure.

3.4.2. At-work CO-FTIR experiments

The diversity in selectivity patterns obtained with the $Rh/M@Al_2O_3$ model catalysts makes them a particularly suitable system for gaining insight into the distinct reaction mechanisms toward each type of reaction product during the SSO. At-work CO-FTIR is a powerful characterization technique, since it offers information both on the nature of metal sites and on CO adsorption modes, as well as on the forming species and reaction intermediates [68,69]. For this study, three catalysts were selected as representative of different selectivity patterns (Table 4), namely $Rh/Sm@Al_2O_3$, producing mainly methanol, $Rh/Pr@Al_2O_3$, displaying a higher selectivity to higher (C_{2+}) alcohols, particularly to ethanol, and $Rh/Ta@Al_2O_3$, chiefly producing hydrocarbons and carboxylic compounds within the oxygenates. These catalysts were reduced in situ in the IR cell and exposed to a syngas flow at different temperatures (RT–553 K) and different times on stream (TOS) at the final reaction temperature of 553 K. The corresponding spectra are given in Figs. 10 and 11 ($Rh/Sm@Al_2O_3$), S5 in the Supplementary material ($Rh/Pr@Al_2O_3$), and 12 ($Rh/Ta@Al_2O_3$).

Qualitatively, the CO-FTIR spectra at RT were similar to those obtained during the low-temperature CO adsorption experiments. Before the peculiarities of each catalyst are individually analyzed, some general trends will be commented on. On one hand, lanthanide carbonate species (characterized by IR bands at about 1500 and 1400 cm^{-1}), which were detected in the original spectra of untreated $Rh/Sm@Al_2O_3$ and $Rh/Pr@Al_2O_3$ samples, became decomposed during the H_2-reduction treatment, as they were no longer observed in the spectra of the as-reduced samples (see, for instance, the spectrum for as-reduced $Rh/Sm@Al_2O_3$ in Fig. 10). Besides, after admission of syngas to the cell at RT, all the samples analyzed showed three main bands in the metal carbonyls region,

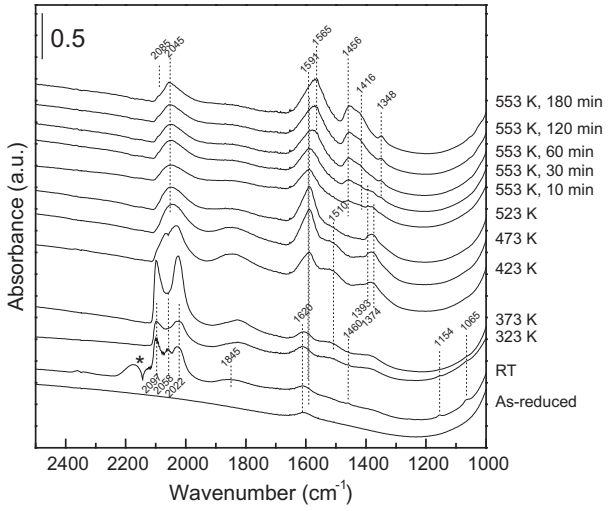

Fig. 10. CO-FTIR spectra for the in situ reduced (H_2, 573 K) $Rh/Sm@Al_2O_3$ catalyst under synthesis gas flow at increasing temperatures (RT–553 K) and different times on stream at 553 K. (∗: CO in the gas phase).

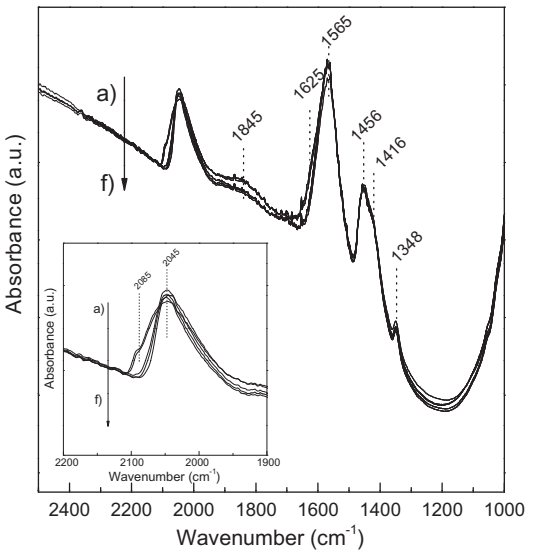

Fig. 11. CO-FTIR spectra for Rh/Sm@Al_2O_3 during the progressive outgassing (a → f) of the IR cell under dynamic vacuum after 3 h on stream at the reaction temperature 553 K under syngas flow.

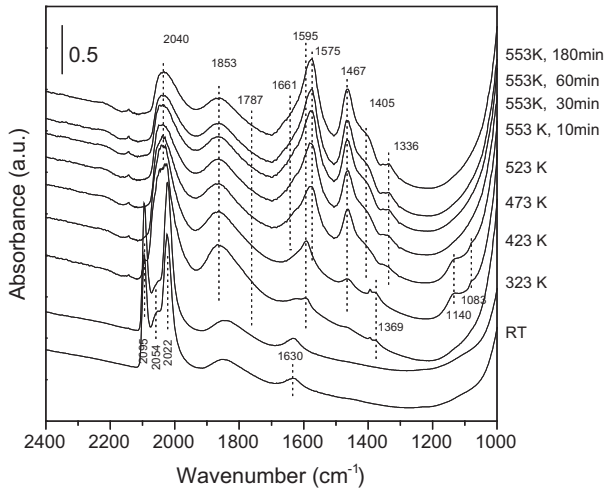

Fig. 12. CO-FTIR spectra for the in situ reduced (H_2, 573 K) Rh/Ta@Al_2O_3 catalyst under synthesis gas flow at increasing temperatures (RT–553 K) and different times on stream at 553 K.

whose assignments have been discussed previously: the doublet at ca. 2090–2100 cm^{-1} and 2020–2030 cm^{-1} ascribed to *gem*-dicarbonyls $Rh^{I}(CO)_2$, the single band at ca. 2040–2070 cm^{-1} related to $Rh^0(CO)_L$ monocarbonyl species, and the broad signal at 1840–1860 cm^{-1} ascribed to $Rh^0_2(CO)_B$ bridged-type species. Additionally, a fourth IR band at ca. 1787 cm^{-1} related to CO adsorbed in the tilted mode was evidenced only for Rh/Ta@Al_2O_3 (Fig. 12). For all three studied samples, increasing the temperature from ambient (RT) to 473 K resulted, on one hand, in the gradual disappearance of the bands associated with *gem*-dicarbonyl species while the monocarbonyl band was left unaffected and, on the other hand, in an increase in the proportion of bridged-type adsorption sites. Moreover, a new bridged-type component was apparent at lower frequencies (1809 cm^{-1}) besides that peaking at 1877 cm^{-1}, as seen, for instance, in the at-work spectra of sample Rh/Pr@Al_2O_3 given in the inset to Fig. S5. These bands have been assigned in the previous literature to different crystallographic facets of Rh, Rh(1 0 0) and Rh(1 1 1) [70]. According to our in situ XPS study, both oxidized and metallic Rh species were present on the catalyst surface under reaction conditions, and therefore the disappearance of the band related to *gem*-dicarbonyls with the increase in temperature during the at-work FTIR experiments should be ascribed to a lower thermal stability of such species than of the linear monocarbonyls. Nevertheless, the increase in the amount of bridged-type species together with the appearance of a new component at lower frequencies could be an indication of a change in the particle size and/or morphology of the supported Rh^0 NPs. Thus, a subtle surface reconstruction of the Rh^0 NPs, exposing both Rh(1 0 0) and Rh(1 1 1) crystallographic facets during catalysis, may be inferred from the at-work IR results reported here, despite no evidence for this being found during the (less surface-sensitive) in situ XPS measurements.

The common trends having been described the particular features for each catalyst will be now discussed. In the case of Rh/Sm@Al_2O_3 (Fig. 10), two IR signals at 1065 and 1154 cm^{-1}, along with an additional weaker band at 1460 cm^{-1}, which are related to adsorbed methoxy species (CH_3O–) [71], and an IR band at 1620 cm^{-1} ascribed to H_2O deformation were perceived in the temperature range of RT–373 K. At higher temperatures (373–523 K), intense bands at 1591 and 1374 cm^{-1} associated with the ν_a(OCO) and ν_s(OCO) vibrations of adsorbed formate species (HCOO–) [72] were also detected. As discussed in Section 3.3, this catalyst produced mainly methanol (Table 4). Therefore, it is reasonable to assume that methanol could be formed by hydrogenation of the adsorbed methoxy groups, although formate species have also been proposed as intermediates for the methanol synthesis [73–75]. At temperatures above 523 K, bands at 1565, 1456, and 1348 cm^{-1} were recorded, which are consensually assigned to ν_a(OCO), ν_s(OCO), and $\delta_s(CH_3)$ vibrations, respectively, in adsorbed acetate species (H_3CHCOO–) [76]. At the reaction temperature of 553 K, the intensity of these bands progressively increased with TOS, suggesting that the acetate species accumulate on the catalyst surface during catalysis. An analysis of the metal carbonyl spectral region at the reaction temperature of 553 K showed the presence of a broad and prominent band peaking at 2045 cm^{-1} (with a shoulder at ca. 2085 cm^{-1}) due to $Rh^0(CO)_L$, along with a very weak IR signal at 1845 cm^{-1} ascribed to the bridged adsorption on the Rh^0 NPs. The high frequency of the 2085 cm^{-1} shoulder is the result of decreased electron back-donation to the CO molecule by Rh surface sites.

The relative stability of the different adsorbed species was also studied, and the results are shown in Fig. 11. As seen there, the signals related to the acetate species were not altered under dynamic vacuum conditions (10^{-7} mbar), indicating that they were strongly adsorbed onto the catalyst surface and thus reinforcing their role of spectators. This result is in contradiction to that previously reported by other authors, who proposed acetates as intermediate species in the SSO reaction [77,78]. Conversely, in line with our results, some researchers assigned the role of spectators to the acetate species [79]. In the metal carbonyl region, only the $Rh^0_2(CO)_B$ band at 1845 cm^{-1} and the shoulder at 2085 cm^{-1} experienced a decrease in intensity, while the IR band at 2045 cm^{-1} remained stable upon evacuation (Fig. 11). This points to the fact that the $Rh^0(CO)_L$ sites peaking at 2045 cm^{-1} do chemisorb CO strongly and thus are not likely to be involved in the reaction mechanism. Conversely, the 2085 cm^{-1} Rh^0 sites are probably involved in catalysis, due to their reversible CO adsorption.

On the other hand, Rh/Pr@Al_2O_3 (Fig. S5) showed behavior qualitatively in agreement with that already discussed for Rh/Sm@Al_2O_3. Both catalysts showed high selectivity toward oxygenates relative to hydrocarbons, though that promoted by PrO_x displayed a higher selectivity to C_{2+} alcohols within the oxygenated products (Table 4). The main spectroscopic difference between Rh/Sm@Al_2O_3 and Rh/Pr@Al_2O_3 was the development of a broad and weak

IR band at 1704 cm^{-1} in the later. In this spectral region ν(C=O), vibrations of carbonyl groups in aldehydes and ketones are registered and, in fact, a band located at 1720 cm^{-1} has been described by Sachtler et al. [78] for acetaldehyde adsorbed onto Rh–Mn/SiO_2. Furthermore, Hindermann et al. [71] assigned a band at ca. 1670 cm^{-1} to formyl species (CHO–) adsorbed onto Rh/CeO_2 and Rh/Pr_6O_{11} catalysts during the catalytic decomposition of methanol. Accordingly, the 1704-cm^{-1} IR band can be ascribed to C=O bonds in adsorbed acyl species. The specificity for this band of Rh/Pr@Al_2O_3 during the at-work experiments suggests that these species may be involved in the formation of C_{2+} alcohols. Indeed, its detection from the temperature range of incipient catalysis, as well as its low and constant intensity, pointing to the absence of accumulation on the catalyst surface, suggests its active participation in the reaction mechanism, though their identification as possible reaction intermediates would deserve further studies.

With regard to the metal carbonyl region, the $Rh_2^0(CO)_B$ band (ca. 1850 cm^{-1}) was hardly visible in the at-work PrO_x-promoted sample, while linear carbonyls peaking at 2054 cm^{-1} predominated. In this spectral region, the main difference between Rh/Sm@Al_2O_3 and Rh/Pr@Al_2O_3 was the absence of the high-frequency component (2085 cm^{-1}) in the latter. Hence, it seems plausible that this type of Rh^0 sites, for which decreased electron back-donation to CO is expected from their higher CO frequency, might be related to the superior selectivity toward methanol afforded by Rh/Sm@Al_2O_3. In fact, decreased electron back-donation has already been suggested to facilitate the nondissociative activation of CO on alternative Pd-based catalysts [56]. The results obtained in the present work, however, do not allow unambiguously clearing up the reason behind the predominance of this kind of sites in the catalyst promoted by the most electron-donating oxide (SmO_x).

Finally, the specific features for the Rh/Ta@Al_2O_3 catalyst will be analyzed. As shown in Fig. 12, formate species (IR bands at 1595 and 1369 cm^{-1}) and water (1630 cm^{-1}) were formed in the low-temperature range (RT–373 K) and then desorbed as the temperature was increased. At increasing temperatures (423–523 K), bands ascribed to methoxy groups (1083 and 1140 cm^{-1}) and carbonyl (C=O) species (1661 cm^{-1}) were observed. At a reaction temperature of 553 K, bands of acetate species (1575, 1467, and 1336 cm^{-1}) and carbonyl compounds predominated in the IR spectra, while the bands related to methoxy species were not longer observed. It is likely that at least some of these ν(C=O) and ν(C–O) signals belong to ester-type adsorbed species (RHCOOR′), in line with the higher selectivity to methyl and ethyl acetates within the oxygenate fraction displayed by the Rh/Ta@Al_2O_3 catalyst (Table 4). The present observations do not allow proposing a reaction mechanism for the formation of carboxylic compounds as major oxygenates, which might involve a concert between Rh sites and acidic sites associated with TaO_x species (and, in general, to Lewis acidic promoters), and further work is in progress to elucidate this aspect, which is out of the scope of the present study.

Additional specific features were apparent in the spectral region of metal carbonyls for Rh/Ta@Al_2O_3 at the synthesis temperature (553 K). On one hand, the ν(CO) signal for bridged–adsorbed CO (band at ca. 1853 cm^{-1}) was significantly more intense than for the formerly analyzed lanthanide-promoted samples. On the other hand, the component at 1787 cm^{-1} related to CO adsorbed in a tilted configuration at the Rh–TaO_x boundary still persisted at the reaction temperature, while the fact the $Rh(CO)_L$ band appeared at lower frequencies (~2040 cm^{-1}) than for the lanthanide-promoted catalysts indicated a higher electron back-donation capacity for the Rh^0 sites in the TaO_x-promoted sample. Interestingly, both linear and bridged carbonyls appeared sensitive to outgassing, suggesting weaker CO adsorption on the Rh^0 sites and thus their dynamic participation in the reaction mechanism. In view of these results, it can be proposed that the higher catalytic activity toward CO dissociation featured by the Rh/Ta@Al_2O_3 catalyst may be ascribed to a higher proportion of $Rh_2(CO)_B$ species and to a higher electron density (i.e., a higher electron back-donation ability) of the Rh^0 surface sites. In fact, some authors have previously suggested that the bridged adsorption mode may favor CO dissociation on Rh^0 NPs [64,80]. Additionally, other factors apart from the nature of the underlying promoter/support might affect the balance in the CO adsorption modes in Rh NPs. In this respect, it has been found that the addition of Ag to supported Rh catalysts both increased the L/B ratio and enhanced the selectivity to oxygenated products [81].

4. Conclusions

A series of model Rh/M@Al_2O_3 catalysts composing a common mesoporous γ-Al_2O_3 carrier having its surface covered by a monolayer of a MO_x promoter (M = Fe, V, Nb, Ta, Ti, Y, Pr, Nd, Sm) was prepared in order to gain insights into promotion effects during the selective synthesis of oxygenates (SSO) from syngas. The as-prepared catalysts featured homogenous metal dispersion (d(Rh) < 3 nm) after activation by H_2 reduction. The series of supported transition metal and lanthanide oxide promoters (MO_x) displayed a wide range of electron-withdrawing/electron-donating capacity (Lewis acidity/basicity) as ascertained by UV–vis spectroscopy coupled with alizarine adsorption. Interestingly, both the specific catalytic activity and the selectivity pattern (as described by the herein defined selectivity parameter Φ) were correlated with the electronic properties of the MO_x oxidic promoters. Thus, while electron-withdrawing oxides promoted CO dissociation, leading to catalysts displaying higher activity and hydrocarbons selectivity, electron-donating promoters favored nondissociative CO insertion events, producing more oxygenated products. CO-FTIR studies on selected catalysts, both in their as-reduced state and under catalysis, pointed to a higher proportion of bridged–adsorbed CO species and a higher electron back-donation capacity of raft-like Rh NPs as responsible for the more favorable dissociative CO activation in catalysts promoted by electron-withdrawing oxides, such as TaO_x. On the other hand, Rh sites displaying decreased electron back-donation were related to the higher nondissociative CO insertion ability afforded by electron-donating oxide promoters, and particularly by SmO_x. The present systematic approach, covering a broad study space, helped in reconciling several previous experimental observations in the Rh-catalyzed synthesis of oxygenates from synthesis gas. It is anticipated that future characterizations will further clear up the relationships between the electronic properties of the oxidic promoters and the morphological-catalytic properties of the promoted Rh nanoparticles.

Acknowledgments

The authors gratefully acknowledge financial support by the Comisión Interministerial de Ciencia y Tecnología (CICYT) of Spain (Project CTQ2007-66614/PPQ). Thanks are also due to Abengoa Bioenergy New Technologies for financial support through the project CENIT I + DEA and for permission to publish these results. The authors are indebted to Dr. M.A. Arribas for performing the CO chemisorption experiments. G. Prieto thanks the MICINN (former MEC) of Spain for an FPU Ph.D. scholarship.

Appendix A. Supplementary material

Supplementary data associated with this article can be found, in the online version, at doi:10.1016/j.jcat.2011.03.025.

References

[1] A.E. Farrell, R.J. Plevin, B.T. Turner, A.D. Jones, M. O'Hare, D.M. Kammen, Science 311 (2006) 506–508.
[2] V. Subramani, S.K. Gangwal, Energy Fuels 22 (2008) 814–839.
[3] R.G. Herman, Catal. Today 55 (2000) 233–245.
[4] J. Rostrup-Nielsen, Catal. Rev. Sci. Eng. 46 (2004) 247–270.
[5] G.W. Huber, S. Iborra, A. Corma, Chem. Rev. 106 (2006) 4044–4098.
[6] J. Spivey, A. Egbebi, Chem. Soc. Rev. 36 (2007) 1514–1528.
[7] M.M. Bhasin, G.L. ÓConnor, Belgium Patent 824822, 1975.
[8] R. Burch, M.I. Petch, Appl. Catal. A 88 (1992) 39–60.
[9] L.E.Y. Nonneman, A.G.T.M. Bastein, V. Ponec, R. Burch, Appl. Catal. 62 (1990) L23–L28.
[10] M. Ichikawa, Bull. Chem. Soc. Jpn. 51 (1978) 2268–2272.
[11] M. Ichikawa, Bull. Chem. Soc. Jpn. 51 (1978) 2273–2277.
[12] Yu-Hua Du, De-An Chen, Khi-Rui Tsai, Appl. Catal. 35 (1987) 77–92.
[13] J. Gao, X. Mo, A.C-.Y. Chien, W. Torres, J.G. Goodwin Jr., J. Catal. 262 (2009) 119–126.
[14] D. Mei, R. Rousseau, S.M. Kathmann, V.-A. Glezakou, M.H. Engelhard, W. Jiang, C. Wang, M.A. Gerber, J.F. White, D.J. Stevens, J. Catal. 271 (2010) 325–342.
[15] T. Matsuzaki, K. Takeuchi, T. Hanaoka, H. Arawaka, Y. Sugi, Appl. Catal. A 105 (1993) 159–184.
[16] V. Ponec, Stud. Surf. Sci. Catal. 64 (1991) 117–157.
[17] T. Nakajo, H. Arakawa, K. Sano, H. Noguchi, S. Matsuhira, Chem. Lett. (1987) 593–596.
[18] H.Y. Luo, P.Z. Lin, S.B. Xie, H.W. Zhou, C.H. Xu, S.Y. Huang, L.W. Lin, D.B. Liang, P.L. Yin, Q. Xin, J. Mol. Catal. A 122 (1997) 115–123.
[19] B.-Q. Xu, W.M.H. Sachtler, J. Catal. 180 (1998) 194–206.
[20] V. Schünemann, H. Treviño, G.D. Lei, D.C. Tomczak, W.M.H. Sachtler, K. Fogash, J.A. Dumesic, J. Catal. 153 (1995) 144–157.
[21] M. Ojeda, M. López-Granados, S. Rojas, P. Terreros, F.J. García-García, J.L.G. Fierro, Appl. Catal. A 261 (2004) 47–55.
[22] M.A. Haider, M.R. Gogate, R.J. Davis, J. Catal. 261 (2009) 9–16.
[23] R. Burch, M.J. Hayes, J. Catal. 165 (1997) 249–261.
[24] A. Boffa, C. Lin, A.T. Bell, G.A. Somorjai, J. Catal. 149 (1994) 149–158.
[25] R.P. Underwood, A.T. Bell, Appl. Catal. 34 (1987) 289–310.
[26] K.P. de Jong, J.H.E. Glezer, H.P.C.E. Kuipers, A. Knoester, C.A. Emeis, J. Catal. 124 (1990) 520–529.
[27] M. Ojeda, S. Rojas, M. Boutonnet, F.J. Pérez-Alonso, F.J. García-García, J.L.G. Fierro, Appl. Catal. A 274 (2004) 33–41.
[28] M.I. Zaki, B. Tesche, L. Kraus, H. Knözinger, Surf. Interf. Anal. 12 (4) (1988) 239–246.
[29] I.E. Wachs, Y. Chen, J.-M. Jehng, L.E. Briand, T. Tanaka, Catal. Today 78 (2003) 13–24.
[30] Damyanova, P. Grange, B. Delmon, J. Catal. 168 (1997) 421–430.
[31] F.J. Gil-Llambías, N. Escalona, C. Pfaff, C. Scott, J. Goldwasser, React. Kinet. Catal. Lett. 66 (1999) 225–229.
[32] M. Bettman, R.E. Chase, K. Otto, W.H. Weber, J. Catal. 117 (1989) 447–454.
[33] T. Yamamoto, T. Tanaka, T. Matsuyama, T. Funabiki, S. Yoshida, J. Phys. Chem. B 105 (2001) 1908–1916.
[34] N.Y. Turova, E.P. Turevskaya, V.G. Kessler, M.I. Yanovskaya, The Chemistry of Metal Alkoxides, Kluwer Academic Publishers, Boston, 2002.
[35] D.I. Enache, E. Bordes-Richard, A. Ensuque, F. Bozon-Verduraz, Appl. Catal. A 278 (2004) 93–102.
[36] J. Sauer, F. Mallow, B. Spliethoff, F. Schüth, Chem. Mater. 14 (2002) 217–224.
[37] M.J. Capitán, M.A. Centeno, P. Malet, I. Carrizosa, J.A. Odriozola, A. Márquez, J.F. Sanz, J. Phys. Chem. 99 (1995) 4655–4660.
[38] N.C. Jeong, J.S. Lee, E.L. Tae, Y.J. Lee, K.B. Yoon, Angew. Chem. Int. Ed. 47 (2008) 10128–10132.
[39] F.P.J.M. Kerkhof, J.A. Moulijn, J. Phys. Chem. 83 (1979) 1612–1619.
[40] J.H. Scofield, J. Electron Spectrosc. Relat. Phenom. 8 (1976) 129–137.
[41] M.P. Seah, Surf. Interf. Anal. 9 (1986) 85–98.
[42] A. Martínez, C. López, F. Márquez, I. Díaz, J. Catal. 220 (2003) 486–499.
[43] D.G. Barton, M. Shtein, R.D. Wilson, S.L. Soled, E. Iglesia, J. Phys. Chem. B 103 (1999) 630–640.
[44] S. Brosda, C.G. Vayenas, J. Wei, Appl. Catal. B 68 (2006) 109–124.
[45] R.T. Sanderson, J. Am. Chem. Soc. 105 (1983) 2259–2261.
[46] V. Dimitrov, S. Sakka, J. Appl. Phys. 79 (1996) 1736–1740.
[47] J. Portier, G. Campet, J. Etourneau, M.C.R. Shastry, B. Tanguy, J. Compd. Alloys 209 (1994) 59–64.
[48] J.A. Duffy, Geochem. Cosmochim. Acta 57 (1993) 3961–3970.
[49] G.R. Gallaher, J.G. Goodwin Jr., C.S. Huang, M. Houalla, J. Catal. 127 (1991) 719–731.
[50] Y. He, G. Chen, S. Kawi, S. Wong, J. Porous Mater. 16 (2009) 721–729.
[51] R.P. Underwood, A.T. Bell, Appl. Catal. 21 (1986) 157–168.
[52] J. Gao, X. Mo, J.G. Goodwin Jr., J. Catal. 268 (2009) 142–149.
[53] H. Yin, Y. Ding, H. Luo, H. Zhu, D. He, J. Xiong, L. Lin, Appl. Catal. A 243 (2003) 155–164.
[54] N.D. Subramanian, J. Gao, X. Mo, J.G. Goodwin Jr., W. Torres, J.J. Spivey, J. Catal. 272 (2010) 204–209.
[55] S.C. Chuang, Y.H. Tian, J.G. Goodwin Jr., I. Wender, J. Catal. 96 (1985) 396–407.
[56] F. Fajula, R.G. Anthony, J.H. Lunsford, J. Catal. 73 (1982) 237–256.
[57] A. Takeuchi, R. Katzer, J. Phys. Chem. 85 (1981) 937–939.
[58] R. Snel, Ind. Eng. Chem. Res. 28 (1989) 654–659.
[59] L.M.P. van Gruijthuijsen, G.J. Howsmon, W.N. Delgass, D.C. Koningsberger, R.A. van Santen, J.W. Niemantsverdriet, J. Catal. 170 (1997) 331–345.
[60] N. Tien-Thao, M.H. Zahedi-Niaki, H. Alamdari, S. Kaliaguine, J. Catal. 245 (2007) 348–357.
[61] H.Y. Luo, P.Z. Lin, S.B. Xie, H.W. Zhou, C.H. Xu, S.Y. Huang, L.W. Lin, D.B. Liang, P.L. Yin, Q. Xin, J. Mol. Catal. A 122 (1997) 115–123.
[62] W.M.H. Sachtler, M. Ichikawa, J. Phys. Chem. 90 (1986) 4752–4758.
[63] B.J. Kip, E.G.F. Hermans, J.H.M.C. van Wolput, N.M.A. Hermans, J. van Grondelle, R. Prins, Appl. Catal. 35 (1987) 109–139.
[64] T. Koerts, W.J.J. Welters, R.A. van Santen, J. Catal. 134 (1992) 1–12.
[65] L.L. Sheu, Z. Karpinski, W.M.H. Sachtler, J. Phys. Chem. 93 (1989) 4890–4894.
[66] A.Y. Stakheev, Y. Zhang, A.V. Ivanov, G.N. Baeva, D.E. Ramaker, D.C. Koningsberger, J. Phys. Chem. C 111 (2007) 3938–3948.
[67] A.Y. Stakheev, L.M. Kustov, Appl. Catal. A 188 (1999) 3–35.
[68] H. Topsøe, J. Catal. 216 (2003) 155–164.
[69] G. Prieto, A. Martínez, P. Concepción, R. Moreno-Tost, J. Catal. 266 (2009) 129–144.
[70] J.C. Lavalley, J. Saussey, J. Lamotte, R. Breault, J.P. Hindermann, A. Kiennemann, J. Phys. Chem. 94 (1990) 5941–5947.
[71] D. Demri, L. Chateau, J.P. Hindermann, A. Kiennemann, M.M. Bettahar, J. Mol. Catal. A 104 (1996) 237–249.
[72] V. Lochař, Appl. Catal. A 309 (2006) 33–36.
[73] J.S. Szanyi, W. Goodman, Catal. Lett. 10 (1991) 383–390.
[74] P.B. Rasmussen, M. Kazuta, I. Chorkendorff, Surf. Sci. 318 (1994) 267–280.
[75] J. Yoshihara, C.T. Campbell, J. Catal. 161 (1996) 776–782.
[76] T. Fukushima, H. Arakawa, M. Ichikawa, J. Chem. Soc. Chem. Commun. (1985) 729–731.
[77] G. van der Lee, V. Ponec, J. Catal. 99 (1986) 511–512.
[78] H. Treviño, T. Hyeon, W.M.H. Sachtler, J. Catal. 170 (1997) 236–243.
[79] R.P. Underwood, A.T. Bell, J. Catal. 111 (1988) 325–335.
[80] K. Fujimoto, M. Kameyama, T. Kunugi, J. Catal. 61 (1980) 7–14.
[81] S.S.C. Chuang, S.I. Pien, J. Catal. 135 (1992) 618–634.